Earth and Space Science

RESEARCH ARTICLE
10.1029/2019EA001066

Geologic Map of Aphrodite Map Area (AMA; I-2476), Venus

V. L. Hansen[1] and I. López[2]

[1]Department of Earth and Environmental Sciences, University of Minnesota, Duluth, Duluth, MN, USA, [2]Department of Biology and Geology, Physics and Inorganic Chemistry, Área de Geología, Universidad Rey Juan Carlos, Móstoles, Madrid, Spain

This article is a companion to López and Hansen (2020), https://doi.org/10.1029/2020EA001171.

Key Points:
- We present a geologic map of the Aphrodite Map Area (0°N–57°S/60–180°E), representing about 13% of Venus' surface
- The map area records three successive geologic eras: the ancient era, the Artemis superstructure era, and fracture zone complex era
- Wrinkle ridges cut many different material units—a condition inconsistent with global catastrophic resurfacing models

Supporting Information:
- Plate S1

Correspondence to:
V. L. Hansen,
vhansen@d.umn.edu

Citation:
Hansen, V. L., López, I. (2020). Geologic map of Aphrodite Map Area (AMA; I-2476), Venus. *Earth and Space Science*, *7*, e2019EA001066. https://doi.org/10.1029/2019EA001066

Received 26 DEC 2019
Accepted 13 JUN 2020
Accepted article online 16 JUL 2020

Abstract We present a 1:10-M-scale geologic map of the Aphrodite Map Area (AMA) of Venus (0°N–57°S/60–80°E). Geologic mapping employed NASA Magellan synthetic aperture radar and altimetry data. The AMA geologic map, with detailed structural elements and geologic units covering over one eighth of Venus' surface, affords an important and unique perspective to test models of global-scale geologic processes through time. Geologic relations record a history inconsistent with global catastrophic resurfacing. The AMA displays a regional coherence of preserved geologic patterns that record three sequential geologic eras: the ancient era, the Artemis superstructure era, and the youngest fracture zone era. The ancient era and Artemis superstructure, with a footprint covering more than 25% of the surface, are recorded in the Niobe Map Area to the north. The latter two eras likely overlap in time. The fracture zone domain, part of a globally extensive province, marks the most spatially focused tectonomagmatic domain within the AMA. Impact craters are both cut by and overprint fracture zone structures. Twelve percent of AMA impact craters that occur within the fracture zone domain predate or formed during fracture zone development. This observation indicates the relative youth of the fracture zone era and is consistent with the possibility that this domain remains geologically active. The AMA records a rich geologic history of large tract of the surface of Venus and provides an important framework to formulate new working hypotheses of Venus evolution and contribute to planning future studies of the surface of planets.

1. Introduction

Nearly 25 years ago, NASA's Magellan mission revealed that Venus lacks plate tectonic processes (Phillips & Hansen, 1994; Solomon, 1993; Solomon et al., 1992), yet Venus' evolution and geodynamic processes remain elusive. Insight into the evolution of Venus and operative geodynamic processes is embedded in the planet surface, laid bare due to Venus' lack of oceans and hydrosphere and thus extensive erosion and/or associated burial by eroded material, and plate tectonic processes that would result in major portions of the lithosphere (and hence surface) being recycled to the mantle. In addition, Venus' dense atmosphere has protected the surface from globally extensive surface gardening by bolide impact—processes that might result in the formation of thick local to regional regolith.

NASA's Magellan synthetic aperture radar (SAR) data provide an unprecedented view of Venus' surface and provide the primary data for the construction of Venusian geologic maps, which in turn form a fundamental database for a wide range of investigations and future exploration. (We use SAR herein to indicate Magellan SAR.)

In this contribution we present a geologic map of the Aphrodite Map Area (AMA) (*I-2476*; 0°N–57°S/60–180°E). A geologic map of the Niobe Planitia Map sheet (*I-2467*; 0–57°N/60–180°E referred to herein as Niobe Map Area [NMA]), adjacent to the AMA but north of the equator, is presented in a separate contribution (López & Hansen, 2020a, 2020b). Geologic mapping of the AMA and NMA were undertaken in a collaborative project. The 1:10-M scale of the AMA and NMA is well suited to the large regional scale of Venus geologic domains (Figure 1) (Hansen, 2018; Hansen & López, 2018). A comparatively similar region on Earth would cover numerous tectonic plate boundaries and include both continental and oceanic crust. The area of the AMA, which covers a 120° longitudinal swath across a latitudinal area comparable to a region of the Earth from the equator to ~10° north of the Antarctic Circle, is large enough to capture tectonic domains, yet small enough to provide a relatively detailed view of geologic relations. Geologic maps, unlike

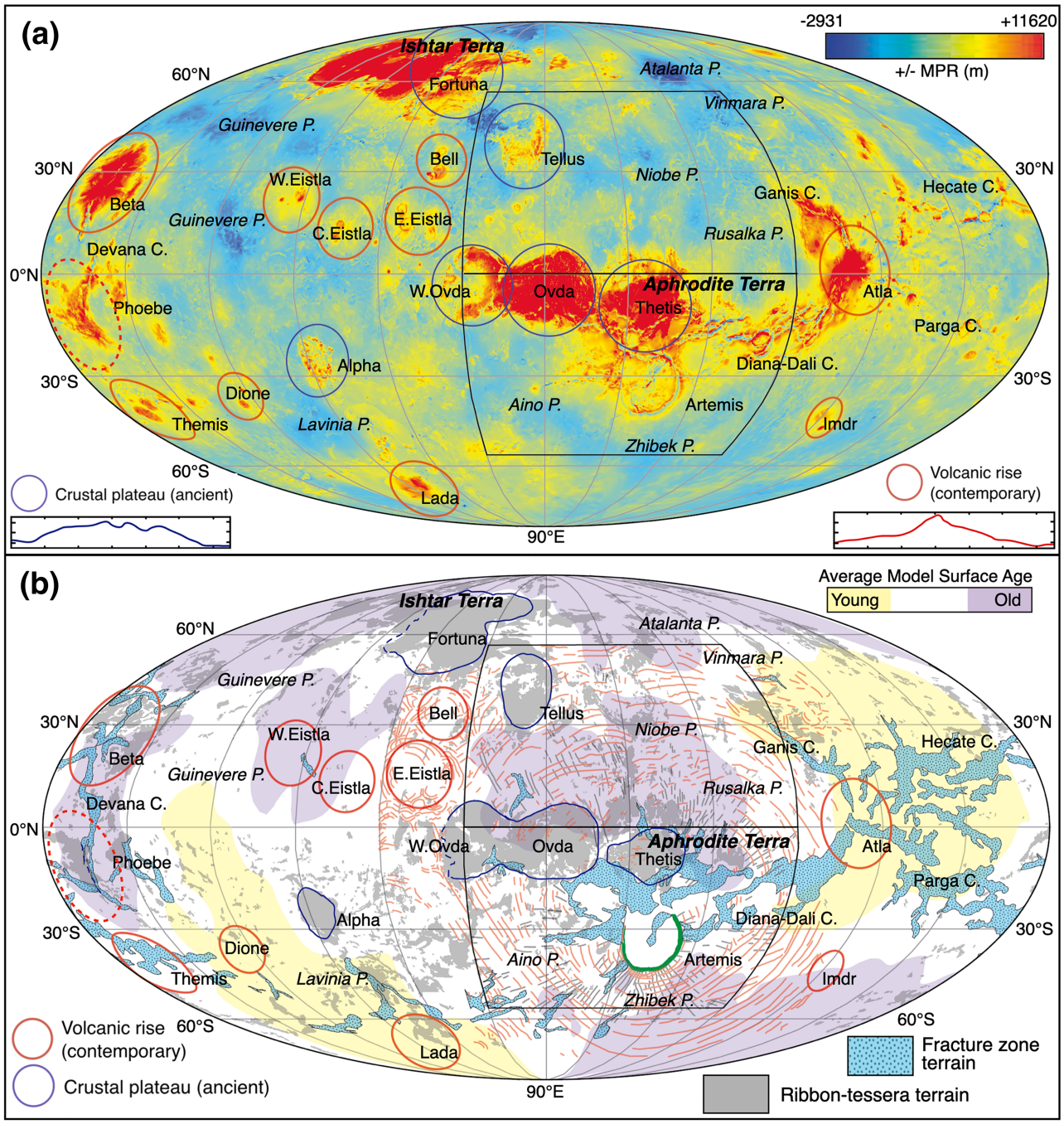

Figure 1. Mollweide projections of Venus; the NMA (north) and AMA (south) are shown as polygons. (a) Altimetry: highlands, red; mesolands, yellow; lowlands, blues; Ishtar Terra and Aphrodite Terra are composite highlands; highland features include crustal plateaus and volcanic rises, and hybrid Phoebe Regio. Planitiae are indicated by "P.," chasmata with "C." Topographic profiles (Ovda Regio, 90°E; Beta Regio 23.6°E), ~6 km vertical, 3,500 km horizontal. (b) Global distribution of average model surface age provinces (Hansen & Young, 2007; Phillips & Izenberg, 1995); fracture zone terrain ("rift" of Price & Suppe, 1995); ribbon-tessera terrain (Hansen & López, 2010); Artemis Chasma (green); and trajectories of Artemis Chasma-radial fractures (gray lines) and wrinkle ridges (faded red lines), including Artemis Chasma-concentric wrinkle ridges and wrinkle ridges not concentric to Artemis (Hansen & Olive, 2010). Labels as in (a). Modified from Hansen (2018).

raw data sets (e.g., SAR, altimetry, and gravity), capture the evolution of a planet's surface. Therefore, geologic maps allow geoscientists to both discover and test models of geologic surface histories and operative geologic processes through time.

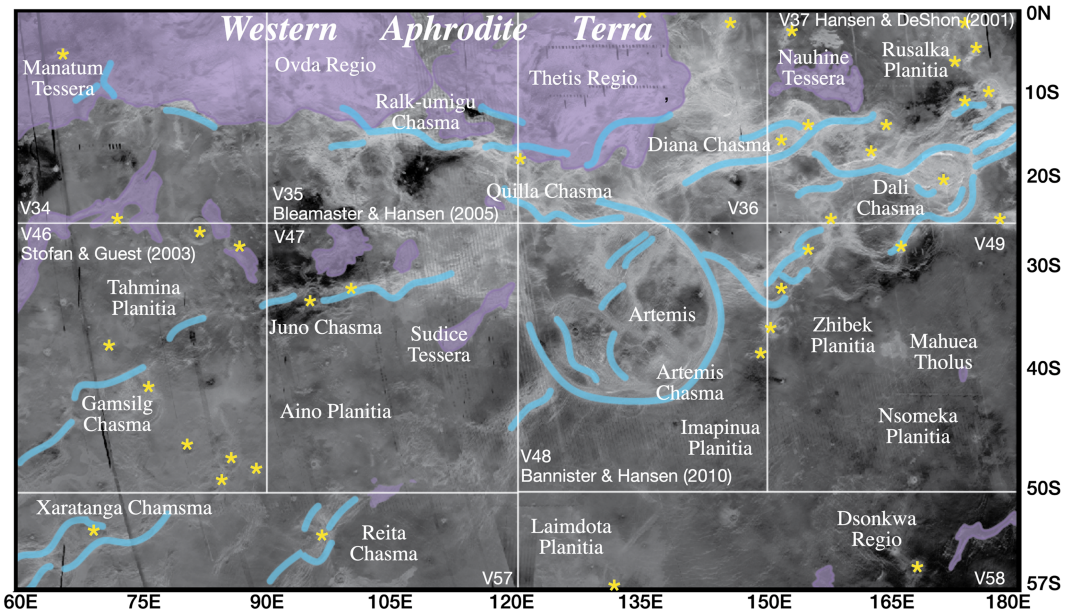

Figure 2. Mercator projection sketch map of the AMA, SAR base with locations. Key: purple, tessera terrain; blue lines, chasmata; yellow stars, coronae; published VMaps in block text.

2. The Aphrodite Map Area

Venus' surface is divided cartographically into 62 1:5-M-scale *VMaps* and eight 1:10-M-scale *IMaps* (https://planetarymapping.wr.usgs.gov/Target/project/Venus). This contribution presents a geologic map of the cartographic defined area I-2476 (U.S. Geological Survey [USGS], 1998) referred to as both the Aphrodite Planitia and Aphrodite Terra Region. Both names are misleading. Aphrodite Terra forms an extensive highland region, but *planitia* refers to lowland; and Aphrodite Terra highland extends beyond *I-2476* (Figure 1). We refer to the region (*I-2476*) as the AMA.

The AMA covers ~60,000,000 km^2 encompassing *western Aphrodite Terra* south of the equator. Aphrodite Terra, characterized by high topography, straddles the equator and consists of a suite of different geologic features including crustal plateaus western Ovda, Ovda, and Thetis Regiones, volcanic rise Atla Regio, the Diana-Dali corona-chasma chain, and Artemis (Figure 1). Artemis Chasma, an ~2,000-km-diameter circular trough south of Thetis Regio, near the center of the AMA serves as a point of geographic reference (Figure 2). Topographically, the AMA ranges from >4 to <7 km relative to mean planetary radius (MPR). Crustal plateaus mark the highest elevations, whereas the lowest elevations fall within Diana and Dali Chasmata. A broad trough (~1,500–3,000 km wide, 1–2 km below MPR) concentric to, but outboard of, Artemis Chasma and separated from the chasma by a broad concentric high (~300 km wide, up to 1 km above MPR) hosts the regional lowlands. The broad trough includes, counterclockwise from the west, Tahmina, Aino, Laimdota, Imapinua, Zhibek, and Nsomeka Planitiae. The Diana-Dali chain cuts the broad topographic trough, with Rusalka Planitia stranded to the north of the other planitiae, marking the northeast corner of the AMA. Manatum Tessera, Xaratanga Chasma, and Dsonkwa Regio anchor the northwest, southwest, and southeast corners, respectively. The AMA displays a regional zone of chasmata with arms of broadly Artemis-radial chasmata in the southwest to the more regionally focused Diana-Dali chain in the northeast (Figure 2).

The AMA contains an assemblage of (1) ribbon-tessera terrain (Hansen & Willis, 1998), and other local basal units; (2) suites of radial and concentric structures associated with the formation of the Artemis superplume (Hansen & Olive, 2010); (3) volcanic material including shield terrain (Aubele, 1996; Hansen, 2005), mons/volcano- and corona-related materials, fracture-fed flows, tholi, and undivided flows; (4) regionally extensive lineament/fracture zones that parallel the corona-chasma chains; and (5) 127 impact craters.

3. Data and Methods

Global data sets collected during NASA's Magellan mission (1989–1994) provide the basis for modern studies of Venus. Ford, Plaut, and Parker (1993) describe Magellan data collection, coverage, and interpretation. The Magellan spacecraft, which carried a 12.6-cm wavelength (S-band) radar system to map the surface of Venus, collected three data sets: (1) SAR surface images, (2) passive microwave thermal emissivity, and (3) altimetric data. High-resolution Doppler tracking yielded gravity observations. Gravity-topography data provide clues to the nature of long-wavelength (hundreds of kilometers) subsurface topographic support. Altimetry data (spatial resolution of ~8 km by ~20 km; vertical resolution of ~50 m) resolve long-wavelength surface features (tens to hundreds of kilometers). SAR data (~100 m/pixel) cover 98% of the surface and provide detailed topographic information suitable for identifying primary and secondary features used for making geologic maps (Hansen & López, 2018; Stofan et al., 1993). Magellan data do not provide robust compositional information.

3.1. Data Employed for Geologic Mapping

The primary data employed in this study, SAR and altimetry data, are available online (Hansen & López, 2020; https://astrocloud.wr.usgs.gov/). SAR Cycle 1 (east-directed illumination, or left-looking) images cover most of the AMA, with local data gaps. Cycle 2 (west-directed illumination, or right-looking) SAR data cover much of AMA, with three main exceptions from west to east (0°N–20°S/65–64°E; 0°N–18°S/123–137°E; 0°N–2°S/155–180°E). Cycle 3 (left-look stereo) SAR data are banded across the AMA and unavailable south of 43°S and from ~93°E to 130°E. Digital Compressed Once Mosaicked Image Data Records (C1-MIDR; 225 m/pixel) SAR data and digital full-resolution radar map (FMAP; 75–125 m/pixel) data were used in constructing the AMA. Ancillary data include Global Topographic Data Record 3 (GTDR 3) with effective horizontal resolution of 10 km and similar products representing Fresnel reflectivity at 12.6-cm wavelength, average 1- to 10-m-scale slope, and derived 12.6-cm emissivity data (GRDR, GSDR, and GEDR, respectively). GTDR data were combined with SAR images to produce synthetic stereo anaglyphs (Kirk et al., 1992) using NIH-Image (National Institute of Health) macros developed by D.A. Young. These images played a critical role in elucidating the relations between flows, primary and secondary structures, and topography.

Although SAR and altimetry data form the foundation for AMA construction, we note here a few observations with respect to ancillary slope, reflectivity, and emissivity data highlighting broad patterns correlative with various features. Slope data (GSDR) values range from 0° to 15° across AMA (Ford, Plaut, Weitz, et al., 1993; Plaut, 1993) the range in values reflects the wide variation in features. Ridges display linear high root-mean-square (RMS) slope values; tesserae correlate with a wormy pattern marked by subdued variations in RMS slope values. Coronae typically show circular RMS slope patterns marked by high to intermediate values, with some coronae showing double RMS slope rings. Planitiae exhibit the lowest and most regionally consistent RMS slope values.

Reflectivity data (GRDR) display a broad range of values. Notable features include tesserae within Ovda and Thetis Regiones, which are extremely bright in contrast to inliers of tessera terrain that correspond to some of the darkest features in the reflectivity data (e.g., Nuahine and Sudice Tesserae). Manatun Tessera (i.e., western Ovda Regio), which sits topographically lower than Ovda and Thetis Regiones (although not in a lowland position), displays reflectivity similar to that of the lowland tessera inliers, although Manatun is quite large relative to the lowland inliers. Chasmata also appear dark in the reflectivity images. Regions of the crustal plateaus with a high density of intratessera flood basin material show intermediate values. Planitiae in southeastern AMA show mostly uniformly intermediate values. Mahuea Tholus is an extremely dark feature.

Emissivity data (GEDR) show tesserae of Ovda and Thetis Regiones as extremely dark, surrounded by regions of intermediate values. Most of the AMA displays intermediate values, with tessera inliers and chasmata-coronae displaying intermediate-high values. Southeastern AMA displays mostly intermediate values; Mahuea Tholus shows intermediate-high values similar to tessera inliers and chasmata.

Tessera terrain within the AMA displays different signatures in slope, emissivity, and reflectivity data as a function of regional elevation. Tesserae in the high-standing Ovda and Thetis Regiones have a similar high-value signature in the slope data to the tesserae of western Ovda (e.g., Manatun Tessera) and tessera-terrain inliers (e.g., Nuahine and Sudice Tesserae); however, Ovda and Thetis Regiones display

low emissivity and extremely high reflectivity compared to low-lying tesserae that display high emissivity and low reflectivity.

3.2. Mapping Methodology

The interpretation of features in SAR images is key to constructing the AMA geologic map. Ford, Plaut, Weitz, et al. (1993) discuss SAR image interpretation in depth. The method employed for defining structural elements and geologic units adheres to historical and contemporary terrestrial mapping methods with particular attention to methods, criteria, and cautions outlined for Venus and employing SAR data (Hansen & López, 2018, and references cited therein).

Magellan SAR data are digital data, which enable mappers to interrogate the data at a wide range of scales, views, and data types throughout the process of geologic map construction. True digital mapping allows a mapper to interact with digital data during the entire mapping process; digital data allow one to zoom in, zoom out, in real time, and to consider different SAR images in order to better understand and unravel the nature of the surface. SAR data over the AMA include multiple look directions and angles; these data can also be combined with each other for stereo images (Plaut, 1993), or with altimetry data for synthetic stereo images (Kirk et al., 1992). We employed each of these data in real time through the mapping processes.

We begin with the delineation of structural elements, both primary (depositional or emplacement-related) and secondary (tectonic), given that these features are most robustly identified in SAR data. Map units represent material emplaced within an increment of geologic history, to which standard stratigraphic methods have some limited application. In contrast, composite units (noted in the description of map units) might not be stratigraphically coherent over the entire represented area and (or) the material may have been emplaced over an extended period of time, particularly in relation to other units and (or) formation of secondary structures. Composite units represent descriptive rather than temporal units. Attempts were made to clearly separate secondary structures from material units; location, orientation, and relative density of primary and secondary structures are shown independent of material units. Evidence for reactivation of secondary structures is common which further complicates the process of unraveling relative temporal constraints and geohistory.

Criteria for distinguishing geologic units include (but is not limited to): (1) the presence of sharp, continuous contacts; (2) truncation of, or interaction with, underlying secondary structures and topography; and (3) primary structures, such as channels or edifice topography that allow a reasonable geologic interpretation and hint at three-dimensional geometry. Some units do not fit these constraints, limiting robust stratigraphic interpretations.

Identification of map units and structural features result in a *relative sequence* of material units *independent of absolute time*. This approach is consistent with terrestrial field geology where rock units and geospatial relations are initially identified independent of absolute time. In terrestrial studies, units might be correlated and fit into a historical framework based on universal (*absolute*) time markers (e.g., fossils, radiometric ages, and paleomagnetic signatures). Currently, there is no means to constrain absolute age on Venus (Hansen, 2000; Hansen & Young, 2007), hampering unit correlation, which requires absolute age constraints. Assessing "absolute" ages of units and determining the duration of formative processes on planetary bodies (save the Moon) currently relies on surface crater density analysis. Given Venus' relatively low global crater density and lack of small impact craters, robust absolute unit age determination is not possible for Venus (Campbell, 1999; Hauck et al., 1998; McKinnon et al., 1997).

Geologic maps constructed using SAR represent high-order derivative products interpreted from multiple views (where possible) of the same surface. Given the side-looking nature of SAR, the specific geographic location of mapped features may vary based on employed SAR images; however, the local- and regional-scale patterns that emerge are robust. Geologic maps constructed using SAR are critical for interpreting Venus geohistories and geoprocesses. Therefore, mapping must be conducted in a fashion that map methodology does not predetermine the resulting geologic map (Hansen, 2000). It is imperative, for example, that secondary structures be distinguished from geologic units, as each record different aspects of geologic histories (Easton et al., 2005, 2016; Hansen, 2000; Wilhelms, 1972, 1990).

All published 1:5-M-scale USGS Venus geologic maps (Figure 2) were consulted during map construction including V35/I-2808 (Bleamaster & Hansen, 2005), V37/I-2752 (Hansen & DeShon, 2002), V46/I-2779

(Stofan & Guest, 2003), and V48/SIM 3099 (Bannister & Hansen, 2010). However, in some cases, map interpretations differ, as happens in the case of geologic mapping on Earth. Discussion of each situation is outside the boundaries of this report.

4. The AMA Geologic Map

This section describes the AMA geologic map (Plate 1; see also Supporting Information Plate S1). We present a broad geologic overview of the four geologic domains and describe primary and secondary structures, geologic units, local and regional tectonic suites, and impact features. Map unit descriptions are included on the geologic map, as is sequence of maps units. Impact crater characteristics are presented in Table 1. A brief geologic history of the AMA completes this report. Feature names referred to herein are shown in Plate 1 (see also Supporting Information Plate S1) and in some cases, in Figures 1 or 2.

4.1. AMA Geologic Setting

The AMA (Figure 2) encompasses the southern part of western Aphrodite Terra, including western Ovda, Ovda and Thetis Regiones, the Diana-Dali corona-chasma chain, and Artemis. Southern AMA is dominated by planitiae that collectively define a broad topographic trough concentric to, but outboard of, Artemis Chasma (Figures 1a and 2). A fan of generally ENE-trending chasmata transect the AMA, with the narrow part of the fan (NE AMA) marked by the Diana-Dali corona-chasma chain. The northern chasmata/fracture zone terrain cuts mostly south of Ovda and Thetis Regiones and north of Artemis (Ralk-umigu and Quilla Chasmata), whereas the fan of chasmata radial to Artemis splays along three zones: Gamsilg and Juno Chasmata, Xaratanga Chasma, and Reita Chasma, counterclockwise from ~8:30 to 6:30. Chasmata are more widely spaced and distributed, and less well defined topographically in the southwest, as compared to Diana-Dali Chasmata. Southeastern AMA, a relatively featureless region, hosts Dsonkwa Regio marked by subdued topography (challenging its "regio" moniker), and Mahuea Tholus notable in its isolation, steep local slopes, and well-defined flow features (Moore et al., 1992).

4.2. Geologic Domains

The AMA is divisible into four geologic domains (1–4) that locally overlap: (1) crustal plateaus (western Ovda, Ovda, and Thetis Regiones) and lowland inliers of ribbon-tessera terrain (Hansen & López, 2010; Hansen & Willis, 1998); (2) the Artemis superstructure marked by a huge dike swarm radial to Artemis Chasma and a wrinkle-ridge suite concentric to Artemis Chasma, 12,000- and 13,000-km diameter, respectively (Hansen & Olive, 2010); (3) the fracture zone complex—broad zones (hundreds of kilometers wide and thousands of kilometers long) of deformation marked by a combination of fractures (broadly defined), coronae, and chasmata; and (4) southeastern AMA, which is cut by Artemis-radial fractures and hosts both shield terrain (Aubele, 1996; Hansen, 2005) and extensive tracts of thin flows cut by Artemis-concentric wrinkle ridges.

4.2.1. Domain 1

Ribbon-tessera terrain (Hansen & Willis, 1998) and other basal regions mark some of the oldest recognizable crustal exposures across the AMA. These are best preserved in elevated crustal plateaus, although exposures occur across much of the AMA preserving an early record of crustal evolution (Hansen & López, 2010); southeastern AMA generally lacks ribbon-tessera terrain, although other basal units occur locally. These basal units could be temporally correlative to ribbon-tessera formation; relative time is unconstrained.

4.2.2. Domain 2

Domain 2, marked by two suites of Artemis Chasma-centric structures—radial fractures and concentric wrinkle ridges—as recognized by Hansen and Olive (2010), occurs across essentially the entire AMA. These two suites of structures and their relations with regional units are best preserved in southeastern AMA, an area relatively unaffected by younger events. In some locations Artemis-radial fractures are well developed; elsewhere, Artemis-concentric wrinkle ridges dominate. Regardless, it is clear that these two suites of concentric and radial structures are genetically related to one another (Hansen & Olive, 2010). Detailed and regional cross-cutting relations indicate that fractures began to form before wrinkle ridges and that the fractures likely served as conduits for Artemis-fed flows (unit Afu) distributing flows locally across huge regional areas. Areas buried by these flows, as well as regions covered by a thin cover of shield terrain (Aubele, 1996; Hansen, 2005), were later deformed by the suite of Artemis-concentric wrinkle ridges. Locally, Artemis-radial fractures are buried, and in some cases these fractures were reactivated as inversion

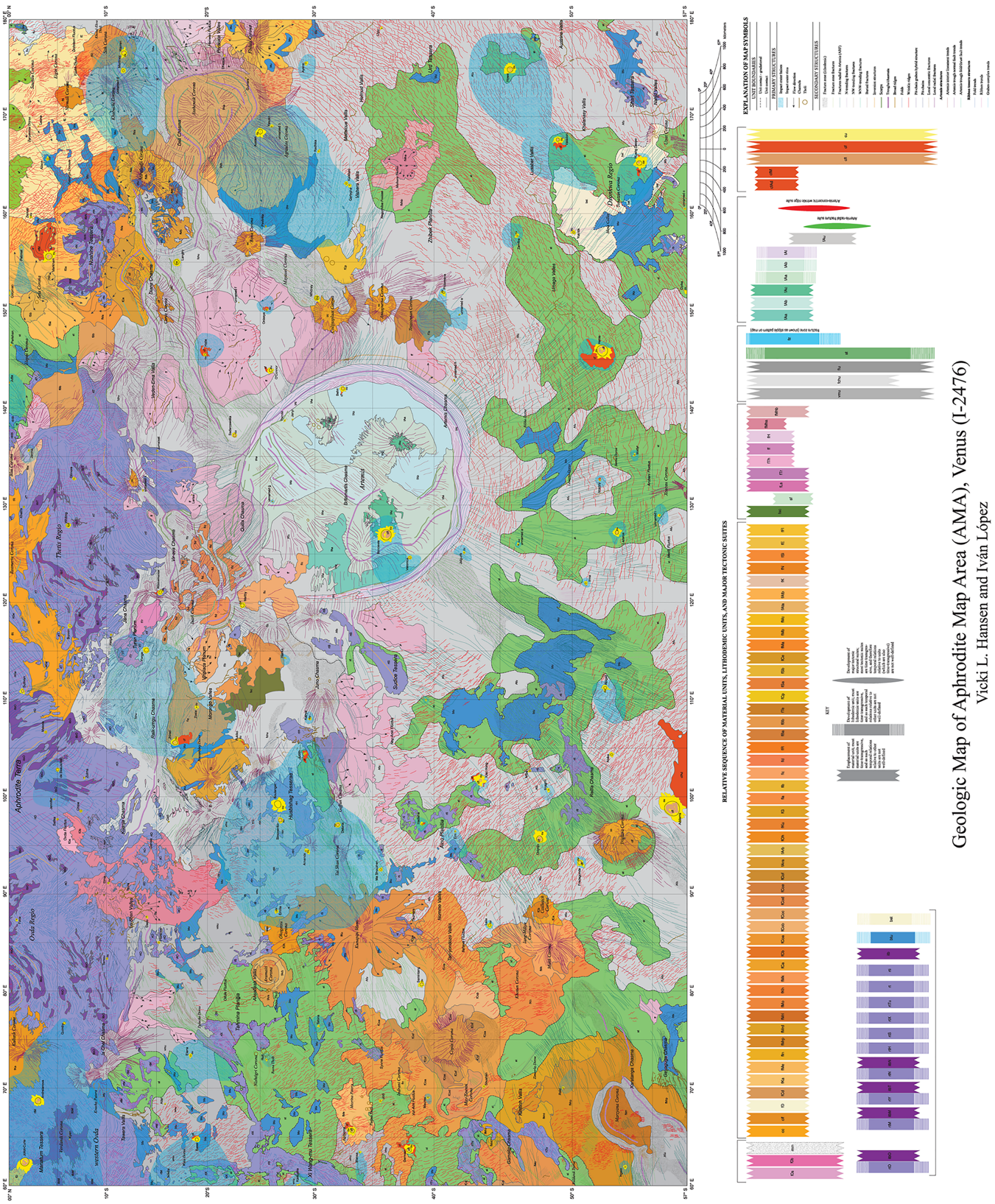

Plate 1. Geologic map of the Aphrodite Map Area (AMA), Venus (I-2467). See also Supporting Information Plate S1.

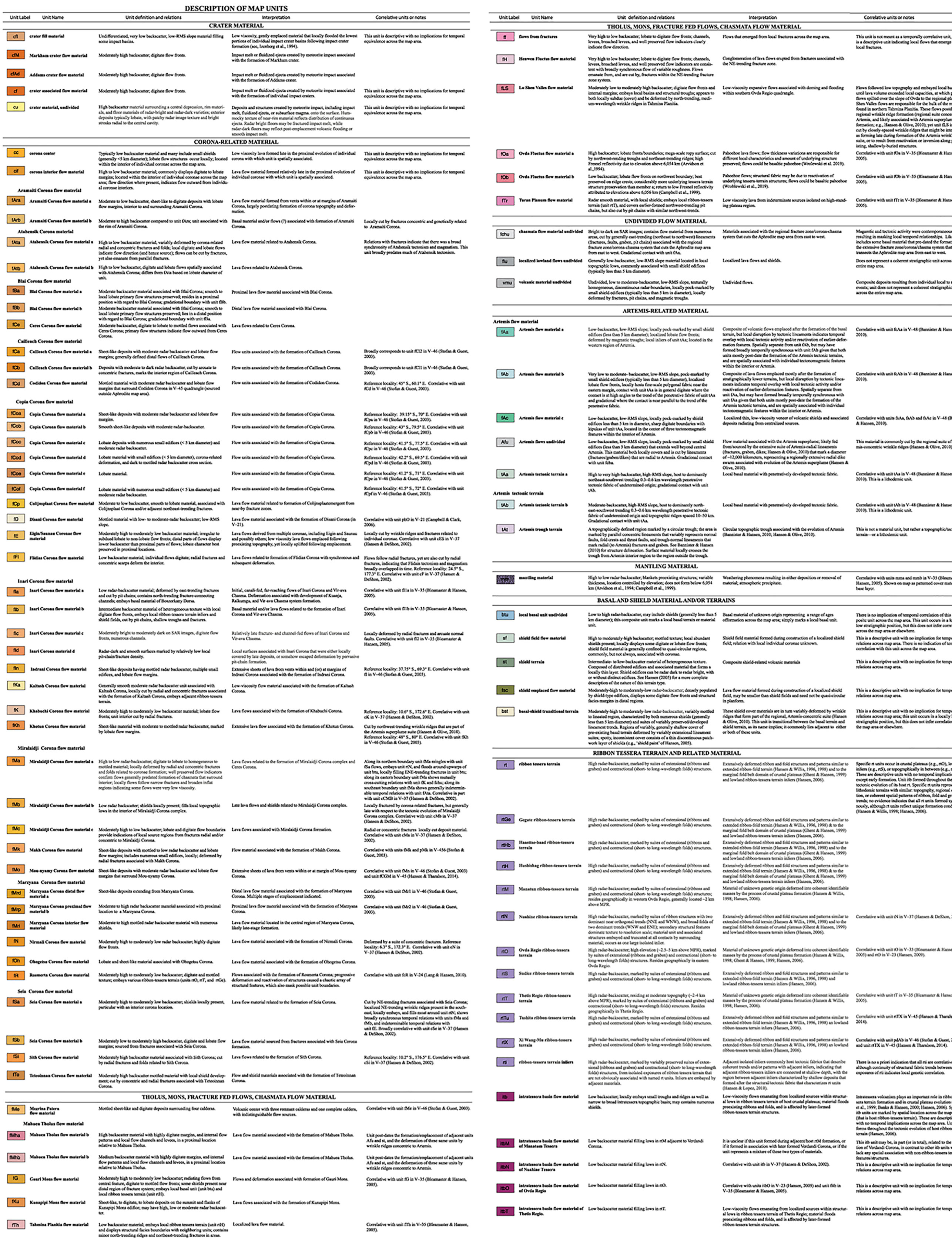

Plate 1. *(Continued)*

Earth and Space Science
10.1029/2019EA001066

Table 1
Aphrodite Map Area Impact Craters

Name	Lat. (°N)	Long. (°E)	Diameter (km)	Elevation (km)	Vmap	Units	Ejecta?	Halo?	Peak?	Rim	Interior fill?	Crater density[a]	Crater database	Deformed?	Temporal implications
Abigail	−52.2	111.2	18.4	6,050.8	57	Afu	Y	N	Y	Y	Y	1.59	H, S	Cut by ARF and ACRW	Predates ARF and ACRW
Abika	−52.5	104.4	14.5	6,051	57	Afu	Y	N	N	Y	Y	2.23	H, S	Cannot tell timing with ACRW	
Addams	−56.2	98.9	87	6,051.5	57	Afu	Y	N	Y	Y	Y	2.86	H, S	Outflows cut by ACRW	Predates ACWR
Afiba	−47.1	102.7	9.5	6,051.71[b]	47	rti	Y	N	N	Y	N	1.59[b]	S	No	
Agrippina	−33.2	65.7	38.6	6,051.1	46	fMe, fu	Y	N	Y	Y	Y	2.55	H, S	Cut by ACRW?	Predates ACWR
Ailar	−15.8	68.4	8.2	6,051.5	34	fu	Y	N	N	Y	N	1.27	H, S	No	
Alison	−4	165.6	14.4	6,051.5	37	btu	Y	Y	Y	Y	Y	2.55	H, S	No	
Amanda	−29.2	94.5	12.5	6,052.1	47	fu	Y	N	N	Y	N	1.91[b]	H, S	No	
Andreianova	−3	68.8	66.1	6,053	34	rtO	Y	N	Y	Y	Y	1.91	H, S	No	
Austen	−25	168.4	45. 1	6,052.5	37/49	fAta	Y	Y	Y	Y	N	2.86	H, S	Cut by Atahensik Corona structures	Predates Atahensik Corona
Ayana	−29.2	175.5	13.8	6,051.9	49	Afu	Y	N	N	Y	Y	2.55	H, S	Unknown	cc
Badarzewska	−22.6	137.2	29.6	6,053.5	36	fchu	Y	N	Y	Y	Y	1.91	H, S	Cuts and cut by FSZ	Formed during FSZ evolution
Bassi	−19	64.6	31	6,051	34	btu, fu	Y	Y	Y	Y	N	1.91	H, S	Buries ACRW	Postdates ACWR
Behn	−32.4	142	25.4	6,052.9	48	fAa	Y	N	Y	Y	Y	1.91	H, S	Ejecta cut by Artemis Chasma faults; interior buries Artemis Chasma faults?	Predates Artemis Chasma; interior flooding postdates Artemis Chasma structures
Blanche	−9.3	157	12.3	6,054.08[b]	37	rtN	Y	N	N	Y	N	1.91[b]	S	tstd	
Bonnevie	−36.1	127	92.2	6,052.4	48	fAa	Y	Y	Y	Y	Y	0.95	H, S	No	Postdates Artemis interior
Bonnin	−6.3	117.6	28.5	6,054.9	35	rtT	Y	N	N	Y	Y	1.27	H, S	No	
Boulanger	−26.6	99.2	71.5	6,052.8	47	rtH	Y	N	Y	Y	N	1.91	H, S	No	
Chiyojo	−47.8	95.7	40.2	6,051.3	47	st	Y	N	Y	Y	Y	2.86	H, S	Covers and cut by ARF; cut by ACRW	ARF predates and postdates crater; crater predates ACWR
Chloe	−7.4	98.6	18.6	6,055.9	35	rtO	Y	N	Y	Y	Y	2.23	H, S	No	
Corpman	0.3	151.8	46	6,052.2	25/37	fSa	Y	Y	N	Y	Y	3.5	H, S	Mostly in Niobe	(Outflows cut by N fractures)
Dado	−13.9	87.6	11.2	6,053.1	34	fLS	Y	N	N	Y	N	1.27	H, S	No	
de Beausoleil	−5	102.8	28.2	6,054.9	35	rtO	Y	N	N	Y	N	2.55	H, S	No	
Deloria	−32	97.1	31.9	6,052.1	47	fu	Y	N	Y	Y	Y	1.91	H, S	Buries fractures	Postdates fractures
Denise	−14.4	94.7	2		35	fLS	Y	N	N	Y	N	—		tstd	
Dheepa	−21.6	176.3	4.7	6,052.6	37	ff	Y	Y	N	Y	N	1.91	H	tstd	
Eini	−41.6	96.4	5.9	6,050.9	47	Afu	Y	Y	N	Y	N	2.86	H, S	tstd	
Elena	−18.3	73.4	17.6	6,051.5	34	fu	Y	N	N	Y	N	1.27	H, S	Buries N-trending fractures	
Elma	−10.1	91.1	10.2	6,054.6	35	fLS	Y	N	N	Y	N	1.91	H, S	tstd	
Emilia	−26.5	88.2	12.5	6,051.6	46	fu	Y	N	N	Y	Y	0.64	H, S	Buries ARF	Postdates ARF
Fava	−0.7	87.4	9.7	6,055.3	34	rtO	Y	N	N	Y	Y?	2.23	H, S	tstd	

Earth and Space Science
10.1029/2019EA001066

Table 1
Continued

Name	Lat. (°N)	Long. (°E)	Diameter (km)	Elevation (km)	Vmap	Units	Ejecta?	Halo?	Peak?	Rim	Interior fill?	Crater density[a]	Crater database	Deformed?	Temporal implications
Florence	−15.2	85	10.5	6,052.9	34	fu	Y	N	N	Y	N	1.27	H, S	No	
Fredegonde	−50.5	93.3	25.2	6,051.6	57	Afu	Y	Y	Y	Y	Y	2.55	H, S	Buries ACRW?	Postdates ACWR?
Fukiko	−23.1	105.8	13.9	6,052.6	35	fG	Y	N	N	Y	Y	2.55	H, S	Outflows bury FZS/CCS	Postdates FZ/CC
Gail	−16.1	97.5	10		35	fchu	Y	N	N	Y	N	—		Cut by FZS	Predates FZS
Germain	−37.9	63.7	35.5	6,051.1	46	st	Y	Y	Y	Y	Y	2.55	H, S	Cut by NW lineaments?	Possibly deformed
Gilmore	−6.7	132.8	21.3	6,055.3	36	rtT	Y	N	N	Y	Y	1.59	H, S	Cut by ARF	Post ttT, pre-ARF
Gulnara	−23.7	174	5	6,051.7	37	fAta	Y	N	N	Y	N	1.91[b]	S	tstd	
Hadisha	−39	97.2	8.9	6,051.3	47	st	Y	Y	N	Y	Y	2.55	H, S	tstd	cc
Halle	−19.8	145.5	21.5	6,053	36	ff	Y	Y	N	Y	Y	1.59	H, S	Covers and cut by FZS/CCS	Formed during FS/CC evolution
Hanka	−27.3	114.3	5	6,053.3	47	fchu	Y	N	N	Y	N	1.59	H, S	No	Postdates FZS
Helga	−10.4	116.7	8.8	6,054.3	35	rtT	Y	N	N	Y	N	0.95	H, S	No	
Henie	−51.9	146	70.4	6,051	58	st	Y	N	Y	Y	Y	1.91	H, S	Buries ARF	Postdates ARF
Howe	−45.7	174.8	38.6	6,051.4	49	st	Y	N	Y	Y	Y	1.59	H, S	Ejecta cut by ACWR?	Predates ACWR?
Huang Daopo	−54.2	165.3	29.1	6,051.9	58	st	Y	N	N	Y	Y	2.86	H, S	Cut by ARF	Predates ARF
Imagmi	−48.4	100.7	7.6	6,050.8	47	Afu	Y	Y	N	Y	N	2.55	H, S	Flows into ARF	Postdates ARF
Irma	−50.9	122	9.5	6,051.2	58	Afu	Y	Y	N	Y	N	2.55	H, S	No	cc
Istadoy	−51.8	132.6	5.4	6,051.2	58	Afu	Y	Y	N	Y	N	2.23	H, S	tstd	
Izudyr	−53.9	135.2	6.6	6,050.9	58	st	Y	Y	N	Y	Y	2.55	H, S	tstd	
Jalgurik	−42.3	125.1	7.5	6,052.5	48	Afu	Y	N	N	Y	N	1.59	H, S	Buries FZS	Postdates FZ
Janina	−2	135.7	9.3	6,053.3	36	fBb	Y	Y	N	Y	Y	1.91	H, S	Buries FZS	Postdates FZ
Janyl	−28	138.8	5.6	6,053	48	fAb	Y	N	N	Y	N	1.59	H, S	tstd	
Jennifer	−4.6	99.8	9.6	6,055.2	35	rtO	Y	N	N	Y	N	2.86	H, S	tstd	
Jhirad	−16.8	105.6	50.2	6,053.5	35	fI1a, btu	Y	N	Y	Y	Y	0.95	H, S	Buries FZS	Postdates FZ
Jodi	−35.7	68.7	10.2	6,051.2	46	st	Y	N	N	Y	N	2.55	H, S	Buries ACRW?	Postdates ACWR?
Joliot-Curie	−1.6	62.4	91.1	6,052.5	34	rtO, itb-M, dD	Y	N	Y	Y	Y	1.91	H, S	No?	Predates dD?
Judith	−29.1	104.5	16.6	6,052.7	47	st	Y	Y	N	Y	Y	2.23	H, S	Buries fractures and canali	Postdates fractures and canali
Jumaisat	−15.1	135.6	7.5	6,054.1	36	rtT	Y	N	N	Y	Y	0.95	H, S	tstd	
Jutta	0	142.6	7	6,052.4	24/36	st	Y	N	N	Y	N	2.23	H	tstd	
Kaikilani	−32.8	163.2	19.9	6,051.8	49	Afu	Y	Y	Y	Y	Y	2.23	H, S	Buries ARF	Postdates ARF
Kastusha	−28.6	59.9	13	6,051.2	45/46	fu	Y	Y	N	Y	N	2.55	H	No	
Katrya	−29.5	108.7	9.2	6,052.6	47	fchu	Y	Y	N	Y	N	1.59	H, S	Buries FZS	Postdates FZ
Khelifa	−1.5	129.9	10.8	6,054.8	36	rtT	Y	N	N	Y	N	1.59	H, S	Cut by ARF	Predates ARF
Kyen	−6.2	64.7	5.2	6,052.7	34	itbM	Y	N	N	Y	?	—	S	tstd	cc
Langtry	−17	155	50.3	6,052.1	37	fchu	Y	N	N	Y	Y	1.59	H, S	Cut by FZS	Predates FZS
Larisa	−18.5	131.1	3.7	6,054.31[b]	36	ff	Y	N	N	Y	N	1.59[b]	S	tstd	
Lazarus	−52.9	127.2	24.2	6,051.3	58	st	Y	Y	Y	Y	Y	2.23	H, S	Buries ARF	Postdates ARF
Leila	−44.2	86.8	18.8	6,051	46	Afu	Y	Y	Y	Y	Y	2.23	H, S	Buries ACRW	Postdates ACWR
Leona	−3.1	169	3	6,051.6	37	fE	Y	N	N	Y	N	2.86	H	tstd	
	−35.7	92.5	18.9	6,051.8	47	Afu	Y	Y	Y	Y	Y	1.59	H, S	Buries ARF and ACRW	Postdates ACWR

Earth and Space Science

10.1029/2019EA001066

Table 1
Continued

Name	Lat. (°N)	Long. (°E)	Diameter (km)	Elevation (km)	Vmap	Units	Ejecta?	Halo?	Peak?	Rim	Interior fill?	Crater density[a]	Crater database	Deformed?	Temporal implications
Ma Shouzhen															
Makola	−3.8	106.7	16.6	6,054	35	rtO	Y	N	N	Y	N	2.23	H	No	
Maltby	−23.3	119.7	36.6	6,053.4	35	fI1b, fIc	Y	N	N	Y	Y	0.64	H	Cut by FZS	Predates FZS
Mansa	−33.9	63.4	8.1	6,051.1	46	fu	Y	N	N	Y	N	2.86	H	tstd	
Markham	−4.1	155.6	71.8	6,052	37	fSa	Y	Y	Y	Y	Y	1.91	H, S	Outflows flow into ARF, bank against ACRW	Postdates ARF and ACWR
Martinez	−11.7	174.7	23.5	6,052.6	37	fK	Y	N	Y	Y	N	0.64	H, S	Covers and cut by FZS	Formed during FZ evolution
Maurea	−39.5	69.1	9.9	6,051.5	46	fCoa	Y	Y	N	Y	Y	2.23	H, S	No	
Ndella	−15.9	60.7	5.9	6,051.2	34	rtM	Y	N	N	Y	N	1.91	H, S	tstd	
Ngaio	−53.3	61.8	9.5	6,052.6	57	fMrdb	Y	Y	N	Y	Y	1.91	H, S	Buries FZS	Postdates FZS
O'Connor	−26	143.9	30.4	6,052.4	48	fchu	Y	N	Y	Y	Y	2.55	H, S	Buries FZS	Postdates FZS
Onissya	−25.6	150.2	8.2	6,052.2	49	ff	Y	Y	N	Y	N	1.59	H, S	Outflows locally buried FZS	Postdates FZS; cc
Opika	−57.1	151.9	9.8	6,050.8	58	st	Y	N	N	Y	N	3.18	H	No?	
Parishan	−0.2	146.5	6.8	6,052.2	24/36	st	Y	N	N	Y	N	2.23	H, S	tstd	Postdates fractures?
Patimat	−1.3	156.5	5.1	6,051.8	37	fSa	Y	N	N	Y	N	1.91	H, S	tstd	Postdates ACWR?; cc
Pavlinka	−25.5	158.7	7.5	6,053.2	49	btu	Y	N	N	Y	N	3.18	H, S	Cut by FSZ/CC	Predates FZS/CC
Philomena	−40.7	151.9	14.8	6,051.6	49	Afu	Y	Y	N	Y	Y	0.95	H, S	Buries ARF; buries ACRW?	Postdates ACWR?
Qarlygha	−33	162.9	9.3	6,051.7	49	Afu	Y	Y	N	Y	N	2.23	H, S	Covers ARF	Postdates ARF
Quimby	−5.7	76.7	23.2	6,054.2	34	rtO	Y	N	Y	Y	N	0.64	H, S	No	Postdates rtO
Radhika	−30.3	166.4	7.9	6,052.3	49	Afu	Y	N	N	Y	N	2.55	H, S	No?	Postdates FZS
Raki	−49.4	70	7.5	6,052.2	46	fMrdb	Y	Y	N	Y	N	1.27	H, S	Buries ARF	Postdates ARF
Ruit	−25.5	72.9	6.4	6,051.3	46	st	Y	Y	N	Y	N	0.95	H, S	tstd	
Safarmo	−10.8	161.4	7.4	6,052.3	37	fMa	Y	N	Y	Y	N	1.91	H, S	tstd	
Salika	−5	97.7	12.5	6,055.5	35	rtO	Y	N	N	Y	N	3.18	H, S	No	
Samintang	−39	80.7	25.9	6,051.4	46	Afu	Y	N	Y	Y	Y	1.91	H, S	Buries ARF	Postdates ARF
Shushan	−43.8	70.2	8.5	6,051.5	46	fCoa	Y	N	N	Y	N	1.91	H, S	Cut by ACRW	Predates ACWR
Simonenko	−26.9	97.6	31.9	6,052.5	47	fu, fTh	Y	Y	Y	Y	Y	1.91	H, S	Buries NE fractures	Postdates NE fractures
Sullivan	−1.4	110.9	32	6,052.6	35	rtO	Y	N	Y	Y	Y	1.27	H, S	No	
Tehina	−30.4	76.4	5.4	6,051.1	46	st	Y	N	N	Y	N	1.27	H, S	tstd	
Temou	−10	83.4	9.3	6,055.2	34	rtO	Y	N	N	Y	N	1.91[b]	H, S	No	
Teumere	−38.3	88.1	5.4	6,051.1	46	fKu	Y	N	N	Y	N	1.91	H, S	tstd	
Teura	−12.3	90.2	9.3	6,054.4	35	fLS	Y	N	N	Y	N	1.27	H, S	Cut by lava channel	Predates lava channel
Ulpu	−35.7	179	7	6,051.5	49	Afu	Y	N	N	Y	N	1.27	H, S	tstd	cc
Unnamed a	−46.3	125.6	5.4	6,051.8	48	st	Y	Y	N	Y	N	2.23	H, S	tstd	
Unnamed b	−26.5	167.9	5.4	6,052.8	49	fAta	Y	N	N	Y	N	2.86	H, S	tstd	
Unnamed c	−56.9	160.5	7	6,051.3	58	st	Y	N	N	Y	N	2.86	H, S	tstd	
Unnamed d	−10.9	173.7	2.7	6,054.5	37	fK	Y	N	N	Y	N	1.27[b]	S	tstd	
Unnamed e	−41.9	149.6	6.4	6,051.7	48	Afu	Y	Y	N	Y	N	0.96[b]	H, S	tstd	

Earth and Space Science

10.1029/2019EA001066

Table 1
Continued

Name	Lat. (°N)	Long. (°E)	Diameter (km)	Elevation (km)	Vmap	Units	Ejecta?	Halo?	Peak?	Rim	Interior fill?	Crater density[a]	Crater database	Deformed?	Temporal implications
Unnamed f	−23	150.9	3.4	6,052.5	37	fchu	Y	Y	N	Y	N	2.23[b]	H, S	tstd	
Unnamed g	−26.1	130.4	6.3	6,053.5	48	fAb	Y	Y	N	Y	N	1.59[b]	H, S	tstd	
Unnamed h	−41.5	142.9	8.2	6,052.3	48	Afu	Y	Y	N	Y	N	0.95	H, S	tstd	
Unnamed i	−55.4	129	14.3	6,051	58	st	Y	Y	N	Y	N	2.23	H, S	tstd	cc
Unnamed j	−39.3	110	6.3	6,051.7	47	st	Y	Y	N	Y	N	0.64	H, S	tstd	
Unnamed k	−13.7	131.6	8.4	6,054.51[b]	36	fl1b	Y	N	N	Y	N	1.59[b]		tstd	
Valadon	−49	167.7	25.2	6,051.7	49	st	Y	N	Y	Y	Y	1.91	H, S	Covers or cut by ARF?	
Veronica	−38.1	124.6	17.9	6,052.4	48	fAb	Y	N	N	Y	Y	1.27	H, S	No?	
Warren	−11.7	176.5	50.9	6,052.4	37	fSi	Y	N	Y	Y	Y	0.95	H, S	Covers and cut by FZ/CC	Formed during FZ/CC evolution
Whiting	−6.1	128	35.7	6,054.7	36	rtT	Y	N	Y	Y	N	1.27	H, S	Cut by ARF?	Predates ARF?
Whitney	−30.2	151.3	42.5	6,052.2	49	fchu	Y	N	Y	Y	N	1.59	H, S	Cut by FZS/CC	Predates FZS/CC
Winnemucca	−15.4	121.1	30.3	6,053.4	36	rtT, fch-u	Y	N	N	Y	N	1.27[b]	H, S	Cut by FZS/CC	Predates FZS/CC
Xiao Hong	−43.5	101.7	38.7	6,050.8	47	Afu	Y	Y	Y	Y	Y	2.55	H, S	Cut by ACRW?	Predates ACRW?
Yasuko	−26.1	169	10.6	6,053.1	49	fAta	Y	N	N	Y	N	2.86	H, S	Covers Atahensik fractures	Postdates Atahensik Corona
Yokhtik	−50.1	158.1	11.4	6,051.7	58	bst	Y	N	N	Y	Y	2.23	H, S	Cut by ARF	Predates ARF
Yomile	−27.3	138.7	13.6	6,053	48	fAb	Y	Y	N	Y	N	1.59	H, S	No	
Yonge	−14	115.1	42.8	6,053.8	35	fchu	Y	N	Y	Y	N	1.27	H, S	Cut by FZS	Predates FZS
Zeinab	−2.2	159.6	12.5	6,051.4	37	fE	Y	N	N	Y	Y	2.86	H, S	Covers ACRW?	Postdates ACWR?
Zemfira	−46.2	157.7	11.4	6,051.3	49	st	Y	N	N	Y	Y	1.59	H, S	No	
Zosia	−18.9	109.2	10.5	6,053	35	fl1a	Y	N	N	Y	N	1.27	H, S	?	
Zulma	−7.7	102	11	6,055.2	35	rtO	Y	N	N	Y	N	1.91	H, S	No	

Note. N = no; Y = yes; ACRW = Artemis-concentric wrinkle ridges; ARF = Artemis-radial fractures; CCS = corona-chasma structures; FZS = fracture zone structures; FZ/CC = fracture zone-corona-chasma; tstd = too small to determine; cc = composite crater. Venus crater databases: S = Schaber et al. (1992); H = Herrick et al. (1997).
[a]Crater density values from Herrick et al. (1997) at a crater's location. Value is the density of craters in the neighborhood of the specified crater; that is, the number of craters (including the specified crater) within a 1,000-km radius circle normalized to give the number of craters per 1×10^6 km^2. [b]Values calculated using the methodology of Herrick et al. (1997).

structures (e.g., DeShon et al., 2000). Artemis-radial fractures locally occur as buried lineaments. Artemis-fed flows lack indications of flow morphology, perhaps due to simple leaking to the surface as a result of the magmatic head intersecting the local surface (Head & Wilson, 1991). These flows were likely characterized by low viscosity, based on the general lack of flow features. Alternatively, flow feature definition was lost through time (e.g., Arvidson et al., 1992).

A broad topographic trough (~6,500-km diameter), concentric to Artemis Chasma, hosts wrinkle ridges within the trough low. Radial fractures are locally preserved in a concentric region on either side of the trough. Collectively, relations indicate that the trough and outer topographic high probably formed during Artemis superstructure evolution with Artemis-fed "flows" occurring more, or collecting within, the broad trough.

4.2.3. Domain 3

This domain cuts diagonally across the AMA from the southwest to the northeast, where it intersects with fracture zones that radiate from the volcanic rise Atla Regio (east of the AMA). Fracture zones, including those in the AMA, recognized in early studies of Magellan global data are referred to as rifts, or rift zones in some published literature (e.g., Price & Suppe, 1994, 1995). However, detailed mapping within portions of these zones indicates that the zones do not record large extensional strain perpendicular to regional fracture trends, as is the case of terrestrial rift zones (Hansen & DeShon, 2002; Hansen & Phillips, 1993). Furthermore, these zones are typically much wider (i.e., normal to trend; locally >2,000 km) than terrestrial rift zones (typically tens of kilometers), and the nature of the linear structures (in map view) within the zones differs from normal faults developed in typical terrestrial rift zones in spacing (extremely closely spaced), shape (extremely straight), and incredible length (hundreds of kilometers). Therefore, we refer to these regions as "fracture zones," following terminology of Hansen and DeShon (2002). The fracture zone domain is characterized by penetratively deformed zones marked by lineaments consisting of fractures, graben, pit chains, stoped troughs, hybrid structures, and coronae and chasmata. The fracture zones and associated structures dominantly postdate the formation of the Artemis-centric fractures and wrinkle ridges. AMA hosts three types of coronae, with hybrids between three end members: (A) coronae marked by concentric structures; (B) radial fracture coronae; and (C) coronae with obvious corona-sourced flows. Radial and concentric fractures represent fractures/graben/dikes and/or magmatic stoping structures; in general, magma locally remained at depth but emerged to the surface in the case of coronae with surface flows. Coronae type may be related to local lithospheric thickness and the ability to support volcanic edifices and surface flows (McGovern et al., 2015).

The fracture/corona/chasma zones define regions of variable deformation along linear to fan-shaped areas with the shape and orientation of each fracture zone broadly paralleling the trend of its internal structural lineament fabric. The most prominent zone, the Diana-Dali corona-chasma chain, trends ENE in the east extending northeast to volcanic rise Atla Regio (outside AMA; Figures 1 and 2); west of Miralaidji Corona this zone splays into two zones. The southern arm trends WSW to SSW marked by the alignment of Bona, Mayauel, Colijnsplaat, Annapurna, and Teteoinnan Coronae. The northern arm extends west through Ceres Corona. West of Ceres the zone splays again, with one arm trending NW to Blai Corona. A more prominent arm, which we refer to informally as the Vir-ava/Ralk-umgu chasma zone, extends westward from Ceres Corona, trending WSW to W and curving to the WNW northwest of Artemis. The Vir-ava/Ralk-umgu chasma zone, which displays extensive development of extremely closely spaced lineaments, includes Quilla, Vir-ava, Jana, Ralk-umgu, and Kuanja Chasmata. Inari Corona lies along this trend between Vin-ava Chasma to the north and Quilla Chasma to the south. Much of the zone cuts south of Thetis and Ovda Regiones, but NW-trending portions dissect tessera terrain both within Ovda Regio and the region between Thetis and Ovda Regiones. Directly north and west of Artemis the Vir-ava/Ralk-umgu chasma zone is characterized by extreme penetrative development of linear troughs and pit chains, which collectively likely represent magmatic stoping (Hansen & López, 2014a, 2014b). The Vir-ava/Ralk-umgu chasma zone is similar in character to the Diana-Dali corona-chasma chain, although it is generally lacking in the development of coronae (with the exception of Inari Corona). The fracture zones take on a different character where the zones dissect ribbon-tessera terrain and crustal plateaus. The lineaments, which are more widely spaced as compared to other portions of the fracture zone, become more difficult to delineate, due in part to the tessera-terrain host and its characteristic ribbon-tessera terrain fabric. A possible north-trending zone anchored by Rosmerta Corona in the south may also form part of a fracture zone, although this zone lies

mostly to the north outside the AMA and is characterized by coronae rather than fractures or other lineaments (Hansen & López, 2018; López & Hansen, 2020a, 2020b).

West of Artemis Chasma, fracture zones take on a fan-like character. One spoke, marked by penetratively developed lineaments, trends SW (7 o'clock relative to Artemis Chasma) and includes Reitia Chasma and Triglava Corona. A second spoke that trends west from Artemis Chasma (9 o'clock) is marked by Juno Chasma, Gefjun and Tai Shan Coronae, and Kunapipi Mons. Southwestern AMA hosts numerous coronae that are broadly aligned along these fracture zones; coronae structures and flows locally mask extensive parts of the fracture zones.

The Diana-Dali arm, which sits along an ~3,000-km-wide linear topographic high that trends toward Atla Regio, is characterized by extremely penetrative deformation across an ~2,000-km-wide band. This zone hosts AMA's largest coronae; associated chasmata form deep troughs marked by steep scarps. These coronae display radial and concentric fractures, with variable development of flows. The easternmost coronae display more flows, whereas fractured surfaces and a notable lack of flows characterize the coronae closer to Artemis. Coronae developed along the fracture zone periphery display more prominent flows, perhaps due more to the lower intensity of deformation than to the nature of the flows. The relatively high elevation across the Diana-Dali belt is consistent with the occurrence of relatively thin lithosphere (Rosenblatt et al., 1994), which is in turn consistent with the formation of coronae characterized by subsurface magmatism, as opposed to surface flows (McGovern et al., 2015). The relative size of the coronae is likely due to the broad width of thin lithosphere (i.e., high elevation)—that is, thin lithosphere across an expansive region allows for the development of large coronae given that the relatively thin lithosphere favors development of coronae (McGovern et al., 2015).

The broad fan-shape region west of Artemis Chasma hosts both coronae and fracture zones; overall deformation here is more distributed or less penetratively developed than in the other fracture zones. We refer to the coronae-fractures zones as spokes given their overall radial geometry with respect to Artemis Chasma. This region is also topographically subdued, consistent with thicker lithosphere (Rosenblatt et al., 1994). Coronae in this part of AMA variably display radial and concentric structures and surface flows. Corona-radial fractures and corona-concentric fractures are best developed along trends parallel to the local orientation of Artemis-radial fractures, or parallel to the trend of the spokes; in contrast, corona-concentric fold suites are best developed parallel to the local orientation of Artemis-concentric wrinkle ridges (i.e., perpendicular to the trend of the aforementioned fracture suites). Most coronae within this region display corona-sourced flows, an observation consistent with a thicker lithosphere across this region (McGovern et al., 2015), compared to that of the Diana-Dali corona-chasma chain, or to the mostly corona-free, Vir-ava/Ralk-umgu chasma zone.

The Vir-ava/Ralk-umgu chasma zone, ~1,000 km wide and up to 3,000–4,000 km long, includes a single corona, Inari. This fracture zone is characterized by extremely penetratively developed (i.e., closely spaced) pit chains, linear troughs, fractures, and hybrid features (section 4.5.2.2). The lineaments are so penetratively developed that host material cannot be defined. However, despite the incredible high lineament density, flows that locally bury earlier-formed lineaments are notably rare (Bleamaster & Hansen, 2004; Tovar et al., 2015).

4.2.4. Domain 4

Southeastern AMA differs from the other domains in that it is defined by area, and a general lack of features. Southeastern AMA is free of crustal plateaus and hosts limited basal terrain and lacks both true coronae and fracture zones. This area preserves an excellent record of the spatial and temporal development of Artemis-radial fractures and Artemis-concentric wrinkle ridges. The limited exposures of basal terrains offer windows in time—providing local, fragmented records of surface evolution prior to the formation of the Artemis superplume. Within Domain 4, Artemis-radial fractures display incredible continuity, extending for 2,000–3,000 km; the structures are locally buried, yet reappear along trend, either as exposed fractures or as veiled, shallowly buried lineaments. Where Artemis-radial fractures are best developed, wrinkle ridges do not form; and where wrinkle ridges are best developed, fractures are clearly buried. Dsonkwa Regio (probably not a true regio as noted previously) hosts Tonatzin and Utset "Coronae" and limited exposures of ribbon-tessera terrain and other basal terrains, which may represent shallowly buried tessera. Tonatzin Corona lacks radial fractures and concentric structures, defined instead mostly

by a shield field; it is not clear why Tonatzin is considered a corona, and this classification should be revisited. However, we preserve the name of Tonatzin Corona herein given that detailed mapping of this feature is outside the scope of the current project. Utset Corona is marked by concentric structures and two suites of fractures, one parallel to local Artemis-radial fractures and another suite near orthogonal to this trend (NNE). Classification of Utset as a corona might also be suspect given its lack of characteristics typical of coronae (e.g., elevated annulus of tectonic structures and an interior depression, Janes et al., 1992; Squyres et al., 1992; Stofan et al., 1992). Dsonkwa Regio marks a slightly elevated local exposure of basal terrain cut by Artemis-radial fractures that is surrounded by thin flows deformed by Artemis-concentric wrinkle ridges. Mahuea Tholus is perhaps the most prominent feature in Domain 4. Urd Tessera, which lies nearly due east of Mahuea Tholus, marks a slightly elevated high characterized by closely spaced NNW-trending folds and NNE-trending lineaments surrounded by younger flows cut by Artemis-concentric wrinkle ridges.

4.3. Primary Structures, Secondary Structures, and Tectonic Fabrics

Structures, both primary (emplacement-related) and secondary (tectonic), are identified in SAR data. Tectonic fabrics represent suites of genetically related secondary structures that together define a coherent structural pattern.

4.3.1. Primary Structures

Primary structures on Venus are mostly related to volcanic features and include channels, shields, pits and pit chains, lobate flow fronts and flow levees, and impact crater haloes and rims (Ford, Plaut, and Parker, 1993). However, some of these features may result from sediment deposition/erosion processes. More detailed work will be required to clarify the formation of all these features.

Channels (or canali) are sinuous, low-backscatter troughs tens to hundreds of kilometers long and a few kilometers wide; locally, they may lack apparent topographic relief and are interpreted to form by channelized fluid flow (Baker et al., 1992, 1997; Komatsu & Baker, 1994). The nature of the fluid is undefined, as is the type of erosion, whether mechanical or thermal, cutting downward from the surface, or upward from depth (e.g., Bussey et al., 1995; Gregg & Greeley, 1993; Jones & Pickering, 2003; Lang & Hansen, 2006; Williams-Jones et al., 1998). Channels could be primary structures, related to levee development during flow emplacement, or channels could be erosional structures in which case they would postdate the emplacement of the units they cut. The formation of these features is not understood (Baker et al., 2015). Multiple mechanisms could contribute to channel formation—that is, channels across the AMA might not share a singular origin (Hansen & López, 2018).

Shields are small (generally 1 to 15 km in diameter, rarely 20 km in diameter), quasi-circular to circular, radar-dark or radar-bright features with or without topographic expression and with or without a central pit, interpreted as small volcanic edifices (Addington, 2001; Crumpler et al., 1997; Guest et al., 1992). The size of individual shields is difficult to constrain because the bases of individual shields are typically poorly defined, and deposits commonly blend smoothly into a composite layer (Hansen, 2005).

Lobate flow fronts and flow levees can indicate local surface flow direction providing information about flow emplacement and local paleo-topography at the time of flow emplacement, unless deposits represent pyroclastic flows (Branney et al., 2002). Flow directions, interpreted from lobate flow fronts and levees, are shown on the map.

Impact craters are perhaps most prominently marked by rims that sit above circular interiors and within/at the boundary of ejecta material that occurs as extremely radar-bright deposits (Wietz, 1993). Impact craters can also display haloes, radar-bright (rough) or radar-dark (smooth) deposits that extend outward from the rim and ejecta deposits up to many crater diameters (Izenberg et al., 1994). Haloes are thought to form as a result of the shock-induced crushing of host material just preceding or accompanying bolide impact or due to accumulation of fine-scale ejecta. Some craters have parabolic haloes, which can extend up to 20 crater radii to the west; these thin deposits are interpreted as due to the interaction of east-to-west zonal winds (Arvidson et al., 1991, 1992; Campbell & Campbell, 1992; Schaller & Melosh, 1998). The nature and extent of impact haloes might be leveraged to provide unique clues about regional geologic histories (Campbell et al., 2015; Whitten & Campbell, 2016).

Crater haloes and parabolic deposits appear to degrade with time losing their radar contrast with surrounding terrain (Izenberg et al., 1994). Impact craters that display both extreme haloes and radar-bright crater interiors are generally interpreted as relatively young, whereas craters with degraded haloes, or lacking haloes entirely, and displaying radar-smooth filled interiors are interpreted as relatively old (Herrick & Rumpf, 2011; Phillips & Izenberg, 1995). Impact crater haloes are indicated on the map with a stippled map pattern so that underlying units and structures can be represented along with the extent of crater haloes.

4.3.2. Secondary Structures

Secondary structures form after the emplacement of geologic units and typically record tectonic processes; accordingly, these structures provide clues for formational tectonic processes. The distribution and (or) character of secondary structures may also provide clues for the delineation of material units, as well as temporal relations between different material units (Hansen, 2000; Hansen & López, 2018; Tanaka et al., 2009). Most radar lineaments represent secondary structures. Stofan et al. (1993) provided an excellent introduction to the interpretation of secondary structures in SAR imagery. Secondary structures within AMA include various types of lineaments, fractures, and faults; pits and pit chains, stoping troughs, and hybrid structures; and folds, ridges, chasmata, and wrinkle ridges. Given that the AMA covers ~60,000,000 km^2, we do not show all lineaments. However, we attempt to capture the essence of recognized structural suites. Therefore, in some cases lineament trends are shown, in other cases each lineament is shown, and in yet other cases a collection of the lineaments is shown; we attempted to balance data, map clarity, and emergent patterns. There is no single unique scale of lineament or feature identification, just as there is not a single unique scale of observation in the case of field-based mapping on Earth, particularly for maps that cover huge areas of Earth's surface.

Fractures are sharply defined lineaments with a negative, or null, topographic signature, commonly grouped into suites based on orientation, pattern (i.e., radial or concentric), and/or spacing (i.e., widely spaced or closely spaced). Fractures are generally interpreted as extensional structures (Banerdt et al., 1997) although there might be very little measurable extension normal to their trends. Locally, fractures consist of en echelon fractures indicative of either a shear fracture origin or the emergence of a fracture at depth to the surface with the en echelon fractures marking hackles. Any consideration of fractures as evidence of tectonic extension should be independently and robustly proven; we do not consider fractures to be extensional structures in the same mode as, for example, normal faults, herein.

Pits—sharply defined depressions, occur individually, or more commonly as pit chains—linear arrays of pits. Pit chains can have a distinctive scalloped plan-view, or be marked by straight, sharply defined parallel walls forming a generally flat-floored trough, given complete connection or coalescing of a chain of pits. Pits or pit chains can be considered primary structures or secondary structures, depending on the question at hand. Pit chains are primary structures relative to pit-related materials, yet they may be secondary structures relative to the units they cut or are emplaced within. Pit chains, which represent regions marked by subsurface excavation, may mark the surface expression of dilatational faults or dikes (Bleamaster & Hansen, 2005; Ferrill et al., 2004; Grosfils & Head, 1994; Okubo & Martel, 1998; Schultz et al., 2004), or they could represent stoping features that would not require associated crustal extension (e.g., Cushing et al., 2015). Pit chains, or stoping troughs, may evolve from fractures, dikes, or faults; these features may or may not result in crustal extension. Pit chains may evolve into shallow troughs, marked by paired, closely spaced (<5 km and commonly ≤1 km) lineaments marking a shallow (tens of meters) flat depression bounded by steep sides; they are interpreted herein as the result of subsurface magmatic activity (e.g., Bannister & Hansen, 2010; Hansen & López, 2018). A full discussion of pit chains and trough structures is outside the goals of this contribution.

Folds are ridges defining wave-like topographic expression marked by a gradational radar character normal to their trend (Stofan et al., 1993). Folds are generally interpreted as contractional structures, although folds locally form in extensional environments in terrestrial settings. Small ridges are topographic ridges with low relief and width (a few kilometers), similar in appearance to folds; these features may or may not be of contractional origin (marked by folds or thrust faults). Large ridges are topographic ridges with moderate relief and width (~5–20 km). Ridges and chasmata (troughs tens of kilometers wide) commonly occur as paired structures within AMA, particularly within the corona/chasma chains and fracture zone domain. Scarps are marked by steep slopes.

Wrinkle ridges define low sinuous spines spaced a few kilometers to tens of kilometers apart and up to a few hundred kilometers long; these lineaments, which represent low (<2%) layer contractional strain, are found on most terrestrial worlds, especially on large flat expanses of volcanic flow materials (Banerdt et al., 1997; Watters, 1988). Wrinkle ridges typically form suites of near parallel structures (and occasionally orthogonal suites) across large regional expanses. Locally within the AMA, wrinkle ridges occur as inversion structures formed by the inversion of buried fractures due to post burial contraction (DeShon et al., 2000); inversion wrinkle ridges typically have straighter less sinuous trends reflecting the nature of their parent fractures.

4.3.3. Tectonic Fabrics

Tectonic fabrics comprise an assemblage of related structural elements that together characterize a rock unit.

Ribbon-tessera fabric is characterized by orthogonally developed suites of ribbons, or ribbon structures and folds. Ribbon structures record layer extension, whereas orthogonal fold suites record layer contraction. Ribbon terrain is marked by parallel bright and dark lineaments that represent periodic parallel ridges and troughs with typical wavelengths of 2 to 5 km (Hansen & Willis, 1996, 1998). Ribbon structures are commonly spatially associated with folds; parallel fold crests and troughs typically trend at a high angle (generally 90°) to ribbon lineaments. These ribbon-tessera folds defined parallel fold suites ranging in wavelength from short (≤1 km), to intermediate, to long (order >10 km); longer wavelength folds host shorter-wavelength folds, carrying them piggyback (Hansen, 2006). Within the AMA we delineate the trends of ribbon-tessera ribbons and folds. Ribbon trends parallel ribbon lineaments, whereas fold trends parallel fold crests or troughs. Together, ribbons and folds characterize ribbon-tessera terrain (Hansen & Willis, 1996, 1998). Graben complexes, an additional possible structural element of ribbon-tessera terrain, typically parallel ribbon trends. Graben complexes are wider and shorter than ribbon structures and thus display smaller length-to-width ratios. Graben complexes that occur within ribbon-tessera terrain typically cut across long-wavelength fold crests, which results in a lens-shape plan view (Ghent & Hansen, 1999; Hansen, 2006). Bindschadler et al. (1992) recognized ribbon, fold, and graben structures within tessera terrain. These workers describe described ribbon structures as "narrow troughs," clearly differentiating ribbon structures from generally parallel but morphologically different graben. Bindschadler et al. (1992) also noted the early formation of ribbons relative to later formed medium- to long-wavelength folds and graben. Some workers do not delineate ribbon structures and graben, which can lead to confusion with regard to the temporal and kinematic evolution of ribbon-tessera fabric (e.g., Gilmore et al., 1997, 1998; Gilmore & Head, 2018), whereas others simply map tessera but do not identify the nature and trend of the tessera fabric structures (e.g., Ivanov & Head, 2011).

Artemis hosts a second type of tectonic fabric within the AMA, as noted by Bannister and Hansen (2010). Artemis interior penetrative fabric represents closely spaced (0.5–1 km) lineaments with slight gradation in radar brightness across strike. The lineaments are interpreted in some cases as short-wavelength low-amplitude folds and in other cases as fracture-like structures; however, in many cases the fabric character is ambiguous given that the fabric approaches the effective resolution (Zimbelman, 2001) of SAR. This distinctive tectonic fabric has, to date, only been recognized within the interior of Artemis. The fabric may be analogous to structural fabric development along terrestrial divergent plate boundaries (see Bannister & Hansen, 2010). Lineament trends are noted for Artemis interior tectonic fabric.

4.4. Map Units

Map units are broadly defined in the following section. The map legend provides a complete description of units (Plate 1).

Contacts between adjacent units vary from sharply defined to gradational, resulting from the low angle nature of individual contacts, and/or the thickness of the units or terrains. For example, shield terrain (unit st) consists of a thin veil of numerous in situ locally sourced deposits associated with individual shields a few kilometers across (Guest et al., 1992; Hansen, 2005); the location of the mapped contact could vary across tens to hundreds of kilometers. The contacts of basal terrain and overlying units also vary from sharp to gradational. Basal terrain cut by fractures and subsequently buried, typically displays sharp contacts marked by fracture truncation. In other cases, the buried lineaments are visible due to thin overlying deposits. The amount/character of fracture burial can also be gradational. Given these relations, and the variation of fracture burial—from no burial to complete burial—the mapped contact (viewed in planform) is typically shown as gradational.

4.4.1. Terrain Units (or Lithodemic Units)

The term "terrain" describes a texturally defined region, for example, a region where tectonism imparted a surface with a penetrative deformation that disallows interpretation of the original unit or units (Wilhelms, 1990). Characteristic terrain texture could imply a shared history, such as a terrestrial tectono-thermal history or an event that melds possibly previously unrelated rock units (any combination of igneous, metamorphic, and sedimentary rocks) into gneissic terrain; no unique history is inferred or required prior to the event(s) that melded potentially separate units into the textural terrain (i.e., lithodemic unit). Events prior to terrain formation are unconstrained in time or process unless specifically noted. Four general classes of terrain units occur across AMA: ribbon-tessera terrain and related material, basal terrain, shield terrain and associate basal-shield terrain transition, and terrain units associated with Artemis Chasma and interior.

Ribbon-tessera terrain and related material are delineated within AMA. Each of these units includes the moniker ribbon-tessera terrain modified by the name of the host tessera region (e.g., Ovda or Thetis ribbon-tessera terrain, rtO and rtT, respectively) or a descriptive term such as inlier of ribbon tessera (rti). The latter terms are used for relatively small exposures or occurrences in unnamed locations. Ribbon-tessera terrain units are differentiated using regional location and structural trends. It is unclear how the various units are related to one another temporally because interpretations of cross-cutting relations are not unique. We also define units associated with ribbon-tessera terrain: intratessera basin material unit itb (see Banks & Hansen, 2000; Hansen, 2006). Similar to unit rt, unit itb is further divided based on location and/or tessera terrain host (e.g., itbO, itbT, and itbN).

Ribbon-tessera terrain typically displays orthogonal ribbon-fold tessera fabric. Fold wavelengths range from less than 1 km—essentially to the effective resolution (Zimbelman, 2001) of SAR for folds, to tens of kilometers. Ribbon wavelengths generally range from 2 to 5 km, although wavelengths locally occur to the effective resolution of SAR. Intratessera basin material (unit itb) commonly fills intermediate- to long-wavelength fold troughs. Unit itb also locally fills short-wavelength fold troughs (not delineated due to scale). See Hansen (2006) for detailed geologic maps illustrating fine-scale fill.

Orthogonal ribbon-fold fabrics are the most common tessera fabric across AMA as they are for ribbon-tessera terrain globally (Hansen & López, 2010). S-C ribbon-tessera fabrics occur locally. S-C tessera fabric, first described by Hansen (1992) and later by Hansen and Willis (1996), shows a fabric asymmetry similar to S-C fabrics within terrestrial ductile shear zones (e.g., Berthé et al., 1979). Both orthogonal ribbon-fold fabric and the S-C tessera fabric occur within ribbon-tessera terrain preserved within crustal plateaus. S-C tessera fabric represents ductile shear zones in central Ovda Regio, along its southern margin and along its eastern margin with Thetis Regio (Ghail, 2002; Kumar, 2005; Romeo et al., 2005; Tuckwell & Ghail, 2003).

Local basal terrains, or local basal terrain undivided, herein, is a term used to describe surfaces that lie within locally low stratigraphic positions relative to exposed adjacent map units. These surfaces share suite(s) of tectonic structures that formed prior to the emplacement of adjacent material; there is no implication of shared histories between spatially separated basal terrain units across the AMA. However, it is possible that isolated (yet adjacent) basal terrain exposures may represent temporally equivalent unconformity bound packages (i.e., allostratigraphic packages).

Shield terrain, first recognized by Aubele (1996), consists of thousands of individual shields and coalesced flow material, referred to as "shield paint" for its apparent low viscosity during emplacement (Hansen, 2005). Shield paint could be formed from any combination of lava flows, air-fall deposits, or pyroclastic flows (Crumpler et al., 1997; Guest et al., 1992). Shield terrain contains material with an interpreted shared emplacement mechanism (represented by primary structures), which differs from ribbon-tessera terrain whose elements include an interpreted shared deformation history (represented by secondary structures).

Within the AMA, shield terrain material (unit st) is marked by distributed small (~1–10 km in diameter) shield edifices and associated local deposits. Unit st generally hosts a high density of shields, although individual shields are not delineated due to map scale, and shield density is difficult to robustly delineate (Hansen, 2005). The contact of unit st with adjacent units can be sharp or gradational over tens to hundreds of kilometers as noted above. Unit st almost certainly represents a time-transgressive unit across the AMA

(e.g., Addington, 2001; Stofan et al., 2005), composed of thousands of local point-source eruptions that may represent point-source, in situ, partial melting (Hansen, 2005). This unit name is descriptive and does not imply temporal equivalence.

Basal-shield transitional terrain (unit bst) marks a transition between basal terrain and stratigraphically higher shield paint, delineated due to its transitional character in which both the basal terrain and shield deposits are apparent.

Three lithodemic terrain units occur within the region including and encompassed by Artemis Chasma: Artemis trough terrain (tAt) and Artemis tectonic terrains, tAa and tAb. The latter correlate with units by the same names originally described by Bannister and Hansen (2010). Artemis trough terrain—defined by trough parallel lineaments that variably correspond to normal faults, thrust faults, and folds crest/troughs—formed during the development of the Artemis trough.

4.4.2. Mantling Material

A mantling material occurs at high elevation locally blanketing ribbon-tessera terrain of southern Ovda Regio. The mantling material occurs as both radar-bright and -dark regions (shown as stipple pattern on host rtO). This unit shows no primary emplacement features and few secondary structures, and display an apparent topographic dependence, and interpreted as elevation limited metal frost deposits (Bleamaster & Hansen, 2005), representing tellurium "snow" (Kerr, 1996; Pettengill et al., 1996) or heavy metal precipitates of lead and bismuth (Schaefer & Fegley, 2004).

4.4.3. Material Units

Material units are geologic materials interpreted to represent emplacement or deposition as a coherent body or entity. Material units can be (1) lithostratigraphic units, which obey the Law of Superposition and mark distinct temporal units (e.g., individual volcanic flows); (2) bounded packages of similar emplacement character but formed at different times (e.g., impact crater ejecta) and thus are not time equivalent; or (3) allostratigraphic, or unconformity-bounded, composite units that cannot be robustly divided given available data and/or map scale.

Artemis-related material encompasses a suite of Artemis interior units fAa, fAb, and fAc associated with tectonomagmatic features (Bannister & Hansen, 2010) and Artemis flows undivided, unit Afu. Unit Afu is the most widely distributed material related to the Artemis superstructure (Hansen & Olive, 2010). Unit fAu extends well beyond Artemis Chasma, covering much of southern AMA; unit fAu both covers and is locally cut by the ~12,000-km-diameter suite of Artemis-radial lineaments (Hansen & Olive, 2010), interpreted as source structures for unit fAu material. Unit fAu is cut by suite of wrinkle ridges concentric to Artemis trough, which record late collapse of the Artemis superplume.

Undivided material includes three units: unit fchu (chasmata flow material undivided), unit flu (localized lowland flows undivided), and unit vmu (volcanic material undivided). Unit fchu is spatially associated with the regional fracture zone/corona-chasma system that cuts AMA from east to west, occurring generally north of Artemis Chasma. Unit fchu shares a gradational contact with unit fAu; the two units are delineated on the basis of spatial location, with unit fchu occurring within the fracture zone regions. This unit likely includes a host of materials including material emplaced prior to fracture zone development (which could include unit Afu), and local flows contemporaneous with and genetically associated with fracture zone evolution. Units flu and vmu are characterized by generally low radar backscatter, low-RMS slope; unit flu occurs in local topographic lows, whereas unit vmu need not be topographically localized. None of these units represent coherent time-specific lithostratigraphic units across AMA.

Tholus, mons, and fracture fed flow material are, as the name implies, material units variably associated with tholus, mons, or fractures. Each unit shows spatially limited extent consistent with a genetic relationship to individual geomorphic features, and the unit name includes the associated feature (e.g., fG, Gauri Mons flow material; fMh, Mahuea Tholus flow material; fH, Henwen Fluctus flow material; and fLS, Lo Shen Valles flow material). Specific characteristics are noted in map unit descriptions. In contrast to the other units, unit ff, flows from fractures, is a descriptive unit—flows fed from fractures—it is not meant as a temporally correlative unit. Unit ff material variably occurs as bright to dark on SAR images with lobate to digitate flow fronts, channels, levees, breached levees, and well-preserved features indicative of flow direction.

Corona-related material and chasmata flow material comprise the largest number of units. Most are corona-related deposits—the majority of which are spatially associated with individual coronae as indicated by the unit name (e.g., fAra, Aramaiti Corona flow a; and fCe, Ceres Corona flow material). Individual characteristics are noted in map unit descriptions (Plate 1). Some coronae have more than one unit delineated; typically, such units are noted with a, b, c, rather than 1, 2, 3. Numerical notation infers temporal constraints, which are typically lacking. In some cases, specific corona flows define more proximal or more distal facies. Location does not carry robust temporal implications, given that distal and proximal facies could develop at different times possibly related to corona evolution stages (e.g., McGovern et al., 2015; Smrekar & Stofan, 1997, 1999). We cannot independently and robustly determine the relative age of flows given the currently available data. It is possible that flow facies formed time-transgressively over the evolution of the host corona. We also map two units not defined as coronae-specific but rather that occur within many coronae—unit cc (corona center) and unit cif (corona interior flow material). Both units occur in the center of coronae, and each likely formed relatively late during the formation of their host corona. Unit cc is typically radar-dark and may include many small shields; unit cif typically displays digitate to lobate flow structures. Both units are descriptive with no temporal equivalence implications across the AMA.

Material unit fcha (chasmata flow material a) is moderately bright on SAR images and with digitate flow fronts, and local shield-type edifices; this unit is only rarely cut by secondary structures and is interpreted as composed of relatively late, generally confined, flows associated with formation of the Kuanja, Ralkumgu, and Vir-ava chasmata systems.

4.4.4. Crater Material

The AMA includes three regionally distributed crater material units (units cfl, cf, and cu). These units are time-transgressive having formed in association with individual impact craters and not as lithostratigraphic packages. Unit cfl represents low viscosity, gently emplaced material that locally fill the lowest portions of individual impact crater basins following, and unrelated to, impact crater formation (Herrick & Rumpf, 2011; Herrick & Sharpton, 2000; Izenberg et al., 1994). Unit cf represents impact melt or fluidized ejecta created by meteorite impact associated with the formation of individual impact craters; exposures are typically small. Unit cu, crater material undivided, includes radar-bright material associated with impact crater formation including crater ejecta and interior deposits.

Units cfM (Markham crater flow material) and cfAd (Addams crater flow material) represent unique flows formed as a result of bolide impact associated with Markham and Addams craters, respectively. The flows could be impact related, fluidized ejecta, or represent tapping of pre-existing subsurface magma, with the latter possibility currently favored.

4.5. Tectonic Structural Suites

Tectonic (or secondary) structures form after the emplacement of a host material unit. Suites of tectonic structures define local and regional patterns that collectively record a shared deformation history and provide clues to operative tectonic or tectonomagmatic processes. We use the terms local and regional tectonic suites to delineate different scales of tectonic suites.

4.5.1. Local Tectonic Suites

Local structural suites are spatially or geometrically associated with specific features such as coronae or montes. Their timing likely corresponds to the formation, or stages of formation, of the features with which they are associated, recognizing that feature development could have been time-transgressive. These suites can be composed of radial fractures (dikes at depth, graben, faults), or concentric fractures, or both. Locally, folds suites form concentric to some coronae. In cases where concentric folds occur, folds generally are developed in north-trending portions of an overall corona-centric pattern, whereas concentric fractures develop along the east-trending portions of the same overall corona-centric pattern (e.g., Copia Corona; 42.5°S/75.5°E). Within the AMA, coronae with radial fracture suites dominate, although some coronae are marked by prominent suites of concentric structures and generally lack radial fracture suites (e.g., Ohogetsu, Aramaiti, Cailleach, and Khotun Coronae). In some cases, local fractures change trend away from the host structure and become parallel to regional trends, reflecting changes in local to regional stress fields (Ernst et al., 1995; López et al., 2008). For example, fractures concentric to Nishtigri Corona (24.5°S/72°E), which are developed best along ENE trends, lose their

concentric geometry away from Nishtigri Corona becoming parallel to the trend of regional fracture zone structures. In the case of Makh Corona (48.7°S/85°E), radial fractures become parallel to regional fracture zone fracture (NE trending). Chasmata and/or troughs also occur spatially associated with many coronae, likely genetically related to their host features (Hansen & Phillips, 1993). Chasmata and ridges are developed concentric to individual coronae, as well as aligned between coronae; in such cases these features broadly define corona-chasma chains. We infer no collective temporal equivalence of local radial and concentric suites across the AMA. (Note: local suites of radial or concentric structures are associated with individual features, but collectively, these tectonic suites can be part of fracture zones and corona-chasma chains.)

4.5.2. Regional Tectonic Suites

Regional structural suites describe coherent patterns across larger areas, lacking specific spatial or geometric correlation with individual features. We identify two suites of regional tectonic structures clearly associated with large-scale features; one group of structural suites is related to the formation of the Artemis superplume (Hansen & Olive, 2010), and the other group is related to the fracture zones and corona-chasma chains. We also delineate three suites of orientation-defined fractures: NW-trending fractures transect southwestern AMA; generally, N-trending fractures are developed in south-central and southeast AMA. Each of these suites occur within large but limited areas and are not obviously associated with other fractures suites.

4.5.2.1. Artemis-Related Structural Suites

Two distinct suites of structures define the Artemis superstructure: fractures that describe a pattern radial to Artemis Chasma with an overall radial fracture diameter on the order of 12,000 km and wrinkle ridges that define a huge regionally developed suite concentric to Artemis Chasma, with an overall suite diameter on the order of 13,000 km (Hansen & López, 2018; Hansen & Olive, 2010; see also Bannister & Hansen, 2010; Hansen, 2002). The fracture suite, here referred to as Artemis-radial fractures, broadly predated formation of the wrinkle-ridge suite, referred to here as Artemis-concentric wrinkle ridges.

Artemis-radial fractures define a suite of fractures radial to Artemis Chasma that cut units in both the AMA and the NMA (Figure 1). The nature of this suite (broadly defined to include fractures, dikes, lineaments, pit chains, and stoping troughs) is particularly well preserved in southeastern AMA (Domain 4) because this region is relatively free of other features. Individual fractures can extend several hundred kilometers. On the map, fractures locally may appear to end where the fracture package intersects ribbon-tessera units due to difficulty in tracing the fractures across these terrains. Such abrupt truncation of the fractures is likely an artifact of mapping. Packages of fractures also locally "end" abruptly where the fractures are buried by younger deposits; elsewhere, the character of the fractures becomes muted, due to shallow burial. Collectively, the fracture suite defines a coherent pattern of radial fractures, with the locus sharing the same center as the locus of Artemis Chasma. Regional patterns of fully exposed fractures delineate exposures of local pre-fracture basal terrain (unit blu). In southeast AMA areas of shallowly buried fractures (?) and a higher density of shields mark a change to transitional basal terrain (unit btu), and truncation of fractures (interpreted as due to burial) marks a transition to local shield terrain (unit st). In this region the map indicates fracture trend but does not delineate buried fractures given differing degrees of apparent burial. Regions where fractures end rather abruptly along trend indicate areas of thicker cover resulting in near complete burial of the (fractured) basal terrain. Artemis-radial fractures are interpreted as having served as feeders for Artemis-related flows (e.g., unit Afu), which were, in turn, deformed by Artemis-concentric wrinkle ridges along with numerous other pre-existing flows.

Some Artemis-radial fractures can be difficult to distinguish from fractures within the fracture zone domain. In general, where fracture zones parallel the trend of the Artemis-radial fracture suite, we designate the fractures as Artemis-radial fractures. Fracture zone spokes mark regions of more focused zones of fracture development. The fracture zone spokes may also have formed after Artemis-radial fractures or out-lasted the evolution of the Artemis-radial fracture suite. Robust detailed temporal relations are unconstrained.

Artemis-concentric wrinkle ridges define a suite of wrinkle ridges concentric to Artemis Chasma with a diameter on the order of 13,000 km (Figure 1). Like the fractures, wrinkle ridges occur at a range of spacing, down to small-scale wrinkle ridges too closely spaced to show on the AMA geologic map; spacing varies with local spacing <5 km.

Wrinkle ridges are notably absent within exposures of ribbon-tessera terrain, even in high-resolution images, although wrinkle ridges occur locally in intratessera basin material (unit itb). Wrinkle ridges occur right up to the contact between ribbon-tessera terrain and surrounding units, such as Afu and st. These relations indicate that ribbon-tessera terrain is not rheologically amenable to wrinkle-ridge formation (i.e., it lacks a thin deformable layer), whereas the thin shield-terrain veneer or unit Afu can readily form wrinkle ridges. Similarly, some exposures of local basal terrain (unit btu) are cut by Artemis-radial fractures but lack wrinkle ridges; thus, these units are not rheologically amenable to wrinkle-ridge formation.

Wrinkle ridges are also absent, or mostly absent, along the fracture zone "spokes" broadly radial to Artemis. The most striking example of this is the Diana-Dali arm, where wrinkle ridges end abruptly to the south of Atahensik Corona in northern Zhibek and Nsomeka Planitiae, and in southern Rusalka Planitia north of Miralaidji Corona. Wrinkle ridges are also mostly absent within the fracture zones in southwestern and western AMA. It is unclear whether this absence results because the fracture zones dominantly postdate wrinkle-ridge suite development, or if these spokes, which typically lie at slightly higher elevations than the surrounding regions, are typically not buried by thin flows, and as such, not rheologically amenable to the formation of wrinkle ridges. Both explanations are possible. Locally, flows associated with coronae in the Diana-Dali region appear to both predate (deformed by) and postdate (bury) Artemis-concentric wrinkle ridges. Corona-flows located at the off-axis distal edges of the fracture zones (e.g., Atahensik, Flidais, and Sith Coronae) are cut by wrinkle ridges.

Artemis-concentric wrinkle ridges also deform many flows associated with individual coronae or montes, particularly in western and southwestern AMA (e.g., Marzyana, Khotun, Cailleach, Makh and Copia Coronae, and Kunapipi Mons). These relations provide clear evidence that the deformed corona/mons-related flows predated formation of this huge wrinkle-ridge suite. Some corona/mons-associated flows do not host wrinkle ridges. These relations might result because the flows formed after the Artemis-concentric wrinkle-ridge forming event or these flows were rheologically not amenable to wrinkle-ridge formation, possibly due to flow thickness, internal flow structure, or composition. For example, most flows associated with Kunapipi Mons (unit fKu) do not show clear development of wrinkle ridges; however, wrinkle ridges clearly cut the distal, and presumably thinner, edges of these flows. More proximal flows might be too thick to form wrinkle ridges, or, alternatively, portions of the Kunapipi flows could postdate formation of the Artemis-concentric wrinkle-ridge suite. In any case, map relations within AMA highlight the challenge of robustly determining temporal relations between flows and regional deformation "events," such as the formation of wrinkle ridges. Clearly, the evolution and construction of a volcanic feature like Kunapipi Mons, and the formation of a regional suite of wrinkle ridges, with a diameter of 13,000 km, are both likely to be time-transgressive, and plausibly, each could last tens to hundreds of millions of years.

Wrinkle ridges formed by inversion occur within Rusalka Planitia (DeShon et al., 2000). Orthogonal patterns of wrinkle ridges in Rusalka Planitia east of Nuahine Tessera are the result of earlier formed Artemis-radial fractures, which were later buried; following burial the filled fractures were closed resulting in inversion of the fracture fill material and the formation of straight (as opposed to sinuous) wrinkle ridges along strike with parts of the fractures that were not buried. Fracture closure and resulting inversion of the fill likely occurred synchronous with the formation of Artemis-concentric wrinkle ridges, which together with the inversion-formed wrinkle ridges, define a suite of orthogonal wrinkle ridges. But it is also possible that the inversion event occurred after (or even before) concentric wrinkle-ridge formation, although synchronous formation would be geologically reasonable.

4.5.2.2. Fracture Zone Structural Suites

Fracture zone structural suites collectively define Domain 3. Lineaments within the fracture zones represent a range of planar structures manifested as lineaments in map view (e.g., fractures, dikes, pit chains, troughs, scarps, stoping troughs, and hybrid structures). Individual zones display different mixes of structural elements, and some include coronae. For example, the Diana-Dali corona-chasma chain hosts numerous scarps and troughs (chasmata) that either parallel the zone or are curvilinear associated with individual large coronae. In contrast, the fracture zone at about 7 o'clock with respect to Artemis Chasma is characterized by extremely closely spaced lineaments and lacks ridges, troughs, and coronae. The Vir-ava/Ralk-umgu chasma zone displays extremely closely spaced lineaments marked by narrow topographic troughs including pit

chains, stoping troughs, or hybrid lineaments and hosts a single corona, Inari Corona. Structural elements within individual fracture zones are likely genetically related, as are the zones.

We delineate a new type of structural element, here referred to as hybrid lineaments, within the fracture zones. The need for this delineation arose given that individual lineaments change along trend, and the effective resolution of the SAR data does not always allow for robust identification of the nature of specific lineaments. Hybrid lineaments, or hybrid structures, are the epitome of tectonovolcanic features; they can change along trend from zones of *en echelon* fractures, fractures, pit chains, graben, leaky dikes, stoping troughs, and channels. Widths range generally from <1 to >5 km; lengths can exceed several 100 km. Lineament spacing ranges from tens of kilometers to lineaments overlapping, intersecting, or coalescing. Hybrid structures can form along trend with other lineaments or result from reactivation of parts of different lineament suites, resulting in a stepped surface pattern, locally forming channels. Hybrid lineaments likely occur throughout much of the fracture zone domain, and because these features occur at the effective resolution of the SAR, many lineaments mapped as fractures could be hybrid lineaments. Although hybrid lineaments locally source flows, evidence of this is relatively rare. More noteworthy is a striking lack of evidence for associated surface flows. The major role of hybrid lineaments appears to be the transfer of material from the surface to depth (rather than from depth to the surface) as evidenced by widespread development of pit chains, and topographic troughs and the lack of evidence for local burial (Hansen & López, 2014b). If these structures transferred a significant amount of material from depth to the surface, then we would expect to observe numerous examples of flooding/filling of troughs by surface flows, burial of troughs, and abrupt truncation of trough lineaments due to burial. However, few such examples exist. If surface eruption was a common occurrence, we would expect that earlier formed structures would be buried and effectively erased from the surface record. However, evidence for a rich history is preserved, consistent with transfer of material to the subsurface. Hybrid structures appear to both predate and postdate various flows, providing evidence of their dynamic role in the extensive volcano-magmatic province of southern Aphrodite Terra. The subsurface nature of these structures remains unknown (i.e., fault, dike, or stoping-dominated); however, the close spacing of the lineaments, the topographic character of steep-sided flat-based troughs, the lack of associated surface flows, and the regional development over areas hundreds of kilometers wide and thousands of kilometers long collectively indicate that these structures are unlikely to be associated with crustal extension (e.g., dikes and/or normal faults). We favor a stoping interpretation (Hansen & López, 2018). Discussion of this topic is outside the scope of the current study.

4.6. Impact Features

AMA hosts 127 impact craters, ranging from 2- to 92.2-km diameter (Table 1). Table 1 lists crater location, diameter, elevation, crater density, host material units, and so forth. Most of the craters are included in existing Venus crater databases (e.g., Herrick et al., 1997; Schaber et al., 1992). Each impact crater displays an interior, rim, and ejecta deposit; about 33% also have parabolic or halo deposits (e.g., Izenberg et al., 1994). Impact craters with rim diameter <14 km generally lack central peaks. Impact crater deposits are shown as unit cu, crater material undivided, representing interior and ejecta deposits associated with local bolide impact. Each impact crater formed during a unique spatial and temporally localized event; therefore, composite unit cu is diachronous across the map area. Over 40% of the craters display radar-smooth interiors, unit cf, interpreted as interior flood deposits that formed after, and unrelated to, initial impact crater formation (Herrick & Rumpf, 2011; Herrick & Sharpton, 2000; Izenberg et al., 1994; Phillips & Izenberg, 1995). For small diameter craters (generally <7 km) the presence of absence or interior fill cannot be confirmed; for craters with diameter <15 km, unit cf is generally not shown on the map. Crater haloes are shown as a stippled pattern.

None of AMA's craters show obvious signs of embayment by flows that breach an individual crater rim; however, this relation does not require that crater formation is the youngest local geologic event. Detailed mapping of Venus impact craters using high-resolution digital elevation models (DEMs) indicates that dark-floored craters with diameter >20 km have an average rim-floor depth of 290 m and rim height (measured from rim to the adjacent surroundings) of 240 m; the depths of these craters are less than that of similar-sized bright-floored craters, indicating significant post-crater volcanic modification of the radar-dark floored craters (Herrick & Rumpf, 2011; Herrick & Sharpton, 2000). Thus, dark-floored craters likely predate, rather than postdate, the emplacement of at least some of the adjacent units (see Herrick &

Rumpf, 2011, for further discussion and Figure 3 of Hansen et al., 2000, for a possible mechanism). The aforementioned DEM study (Herrick & Rumpf, 2011) includes four craters within the AMA (Joliet-Curie, Markham, Langtry, and Warren). Geologic mapping of individual craters using high-resolution DEMs has not been employed in the construction of the AMA.

Temporal relations between craters and tectonic events can be difficult to robustly constrain. If a crater lies between structural elements that comprise the local tectonic suite, such as wrinkle ridges or spaced fractures, the relative timing of crater formation and tectonic activity cannot be determined (Hansen, 2000). Evidence for crater deformation (or lack thereof) is noted in Table 1 in cases where information can be extracted from map relations. At least 23 craters show clear evidence of deformation (and four craters show possible deformation) indicating that at least these craters formed before local tectonic activity ceased. However, an apparent lack of deformation is not a robust positive test for crater formation after local tectonic activity given the spaced nature of tectonic deformation fabrics and the point location of individual craters (see Figure 3 of Hansen, 2000). In addition, craters with diameter ≤7 km are generally too small to be able to robustly determine if the craters are deformed; 27 craters within AMA (20%) have a diameter ≤7 km and therefore cannot be used to evaluate the relative timing of tectonic activity. At least 22% (possibly >26%) of the AMA's craters with diameter >7 km show evidence of deformation. This observation is notable given that the AMA lies fully outside the Beta-Alta-Themis region, which encompasses the area of Venus marked by the lowest crater density and highest percentage of craters obviously modified by tectonic or volcanic activity (e.g., Hansen & Young, 2007; Herrick & Sharpton, 2000; Phillips & Izenberg, 1995).

Specific geological events occurred *after* the formation of some impact craters, as indicated by cross-cutting relations (Table 1). Craters Abigail, Chiyojo, Gilmore, Huang Daopo, Khelifa, Shushan, and Yokhtik appear to be cut by Artemis-radial fractures and/or Artemis-concentric wrinkle ridges; thus, these craters formed prior to the cessation of the Artemis superplume (e.g., Hansen & Olive, 2010). Craters Agrippina and Xiao Hong might also be cut by Artemis superstructure-related fractures and/or wrinkle ridges and therefore could also have predated cessation of the Artemis superplume. In addition, the following craters appear to be cut by fracture zone or corona-chain structures, and therefore, they were likely emplaced broadly prior to (or during) the evolution of the fracture zone domain: Austen, Gail, Langtry, Maltby, Pavlinka, Teura, Winnemucca, Whitney, and Yonge. Langtry crater displays a flooded interior, which is cut by fracture zone structures; therefore, emplacement of the interior crater fill (which formed after the impact crater itself) occurred prior to fracture zone evolution, or at least prior to the end of fracture zone evolution. Our mapping agrees with the detailed DEM study of Herrick & Rumpf (2011; Figures 32 and 33 therein). Austen crater is cut by fractures related to Atahensik Corona, thus predating final formation of Atahensik. O'Connor, Halle, Martinez, and Warren craters both cover and are cut by fracture zone/corona/chasma structures; therefore, these impact craters likely formed at some point during the time-transgressive evolution of the fracture zone domain. Twelve percent of craters large enough to record geologic relations predate, or formed synchronously with, fracture zone structures and/or coronae. This observation indicates the relative youth of the fracture zone domain and is consistent with the possibility that this complex remains geologically active. A nearly equal number of craters (11%) cross-cut local fracture zone structures. Collectively, these observations are consistent with fracture zone domain evolution over a substantial period, given that numerous individual craters predate, formed synchronous with, or postdate fracture zone structures.

Twenty-two craters locally postdate Artemis-related structures or fracture zone structures; therefore, these craters formed after the (local) waning of these tectonic events. At least 10 of the craters have radar-smooth interiors, whereas others have radar-rough (bright) interiors and halo deposits, consistent with relatively young ages (e.g., Izenberg et al., 1994). Collectively, these observations indicate that Artemis-structure and/or fracture zone formation was followed by local impact crater formation with interior flooding of some crater interiors.

Markham and Addams craters in the northeast and southwest AMA, respectively, display impressive outflow deposits. Both formed on regions marked by suites of concentric fractures on the flanks of coronae—Markham on the eastern flank of Seia Corona and Addams on the eastern flank of Triglava Corona. Both impact craters display radar-smooth interiors, and both have possible halo deposits that "mute" adjacent wrinkle-ridge structures; and in both cases, associated outflow deposits likely postdate formation of Artemis-concentric wrinkle ridges. Both impact craters also display butterfly ejecta deposits indicative of

oblique impact (e.g., Schultz, 1992); Markham resulted from impact from the southwest, whereas Addams crater formed due to impact from the northwest. Both craters apparently formed after, or possibly in the late stages of, the formation of Artemis-concentric wrinkle ridges, and hence after, or late during, the waning stages of the Artemis superplume. Both impact craters likely tapped into subsurface magma chambers associated with their respective corona-related structures. Given the location of these impact craters on the flanks of coronae, and their associated outflow material, it is likely that their radar-smooth interiors also relate to their respective locations relative to their host coronae.

The impact crater data and observations, independently and taken together with the observation that >40% of AMA craters show interior flooding, indicate that a significant number of AMA impact craters experienced notable geological events (i.e., interior fill emplacement) after their formation. These results are consistent with the results of analysis of high-resolution DEM data of Venus impact craters that reveal significant geologic modification of numerous impact craters (Herrick & Rumpf, 2011). These results are contrary to initial surveys of the Venus crater population conducted using NASA Magellan data, used to suggest that only a few percent of Venus craters were deformed or embayed by volcanic material (Collins et al., 1999; Herrick et al., 1997; Herrick & Phillips, 1994; Phillips et al., 1992; Schaber et al., 1992; Strom et al., 1994). These new data, along with the Herrick and Rumpf (2011) study, are difficult to accommodate within the context of catastrophic resurfacing models, or with any resurfacing models that require the vast majority of Venus impact craters to mark the top of the stratigraphic column (e.g., Basilevsky et al., 1997, 1999; Basilevsky & Head, 1998, 2000, 2002a, 2002b, 2006; Ivanov & Head, 2015a, 2015b; Kreslavsky et al., 2015; Reese et al., 2007; Romeo, 2013; Romeo & Turcotte, 2010; Solomatov & Moresi, 1996; Strom et al., 1994; Turcotte, 1993; Turcotte et al., 1999). Thus, impact crater relations within the AMA cast doubt on the conclusions of these studies. In addition to the data described herein, a growing number of studies similarly indicate that hypotheses of catastrophic resurfacing, or hypotheses that call for late formation of most impact craters on Venus, are inconsistent with geologic relations and/or modeling (e.g., Bjonnes et al., 2012; Guest & Stofan, 1999; Hansen & López, 2010; Hansen & Olive, 2010; Hansen & Young, 2007; Herrick & Rumpf, 2011; Herrick & Sharpton, 2000; O'Rourke & Korenaga, 2015; O'Rourke et al., 2014) and collectively challenge assumptions that the Venus crater population represents a limited, young, geologic time period.

5. Geologic History

The geologic history that emerges from the AMA is, broadly speaking, relatively simple, although a rich regional history emerges (Figure 3). An ancient era marked by formation of ribbon-tessera terrain and crustal plateaus (and perhaps basal terrain) predated time-transgressive evolution of the Artemis superstructure; Artemis superstructure formation was broadly followed by, more spatially focused, evolution of the fracture zone complex marked by fracture zones and corona-chasma chains. Evolution of the fracture zone complex seems to have broadly outlasted Artemis superstructure evolution.

The broad regional history parallels the three major geological eras identified through structural element mapping across the combined NMA and AMA (Hansen & López, 2018). The three eras—the ancient era, the Artemis superstructure era, and the fracture zone complex era—are discussed briefly below. Basal ribbon-tessera terrain units formed early across AMA and in a time-transgressive manner comprising the hallmark of the ancient era. Not all ribbon-tessera formed in one event, although ribbon-tessera terrain likely formed within an ancient geological era marked by specific geologic conditions, most notably an era marked by thin global lithosphere (Bindschadler, 1995; Hansen, 2006; Hansen & López, 2018; Hansen et al., 2000; Phillips & Hansen, 1994, 1998). Composite yet local basal terrain (unit btu) could have formed before, during, or after the era during which ribbon-tessera terrain formed. Exposures of unit btu mark the oldest (local) exposed surface in each specific area of exposure; however, no data required that isolated exposures are geologically or temporally correlative. The exposures of unit btu are commonly cut by lineaments—mostly fractures, broadly defined. We do not recognize coherent patterns in these lineaments between exposures, unlike ribbon-tessera terrain, in which the structural fabrics are define by a unique and distinctive assemble of structural elements (e.g., Hansen & López, 2010). In some case btu might be buried unit rt.

Artemis, the hallmark of the Artemis superstructure era, includes an interior high, a deep (~2 km) narrow (50–150 km) 2,100-km-diameter trough (Artemis Chasma), outer rise (2,400-km diameter), long-

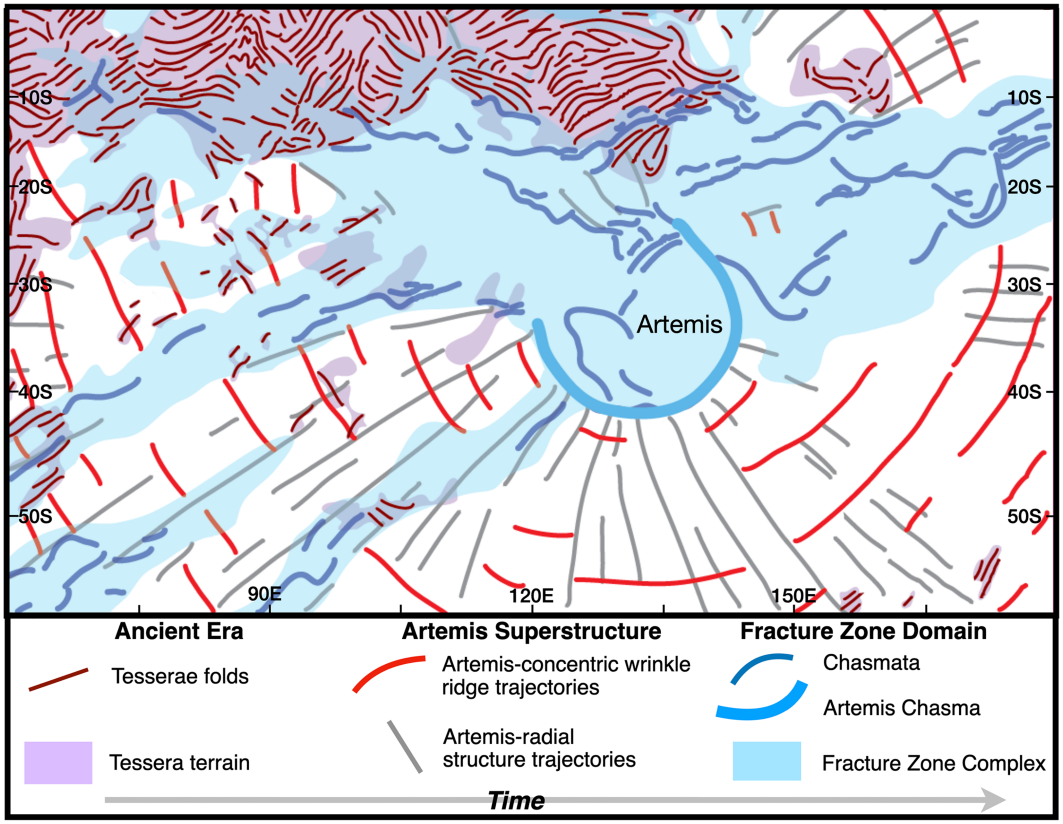

Figure 3. Mercator projection summary of the tectonic regimes within the AMA.

wavelength outer trough (6,500-km diameter), radial dike swarm (12,000-km diameter), and concentric wrinkle ridges (13,000-km diameter). These features record progressive evolution of Artemis, as follows. (1) Initial doming and subsurface magma emplacement accompanied radial fracturing. (2) Fractures (subsurface dikes) propagated laterally, driven by magma buffering, producing dikes with widths and sizes independent of chamber size (Ernst et al., 1995; Grosfils & Head, 1994; Parfitt & Head, 1993). Emplacement of lateral dikes in the constant driving pressure (magma buffered) produced dikes with sizes and widths that are very large and are independent of chamber size. (3) Dike-magma effusion fed local cover deposits (unit Afu), resulting in local burial of some radial fractures. (4) It is likely that an extensive region of the surface was uplifted as a result of superplume structure evolution. (5) Wrinkle ridges deformed the cover deposits (driven by coupling of convective mantle or plume flow to the lithosphere, e.g., Phillips, 1990; Rosenblatt et al., 1994, and/or due to collapse of the huge regional uplift). (6) Late topographic collapse (and/or loading) resulted in formation of the broad outer trough (the trough might also record mantle flow). (7) Artemis Chasma and its interior region mark the decay of the Artemis superplume into a smaller (but still large) plume-type structure, resulting in regional localization of the Artemis interior and chasma (Bannister & Hansen, 2010; Hansen & Olive, 2010).

The fracture zones and corona-chasma chains that define radial spokes relative to Artemis Chasma broadly postdate the formation of Artemis-radial fractures and variably overlap in time with Artemis-concentric wrinkle-ridge formation. In western AMA coronae mostly align along the fracture zones spokes, suggestive of a genetic relationship between coronae and fracture zones. We suggest that these features may have formed in a continuum with the Artemis superplume, perhaps forming in the waning stages of the superplume, and at the same time, or soon after, the Artemis plume came into existence. Evolution of the Diana-Dali corona-chasma chain outlasted the formation of Artemis-concentric wrinkle-ridge suites as evidence by truncation/interruption of the wrinkle ridge trends across this zone. However, as noted, Artemis-concentric wrinkle ridges, which mark collapse of the Artemis superplume, cut some corona-sourced flows in Rusalka, Zhibek, and Nsomeka Planitiae. The picture that emerges is one in

which tectonism (deformation) and magmatic activity became spatially more focused with time. Initially, the Artemis superplume resulted in uplift of a huge circumferential region coupled with formation of radial fractures with a footprint of at least 12,000-km diameter extending north into the NMA (Hansen & López, 2018; Hansen & Olive, 2010; López & Hansen, 2020a). Locally, magma emerged from these radial fractures forming unit Afu. In some regions the radial fractures were reactivated, in some regions the fractures were not covered (similar to regions of ribbon-tessera terrain and local basal exposures which were not buried by these flows), and in some regions, the radial fractures were completely buried by these flows. Formation of the Artemis-concentric wrinkle-ridge suite occurred broadly after formation of the Artemis-radial fractures, but wrinkle-ridge formation was outlasted in turn by more localized spokes of fracture zone development. Some of the fracture zones were dominated by the formation of near-parallel fractures, whereas other zones were dominated by corona-mons formation. Elsewhere, coronae, chasmata, and fractures developed in concert with one another along these fracture zones (e.g., Diana-Dali). With time, the Artemis superplume decayed to the Artemis plume, and Artemis tectonic and volcanic activity became limited to the evolution of the interior of Artemis and Artemis Chasma (see Bannister & Hansen, 2010).

The timing of shield terrain formation, unit st, is probably not the same across the AMA; however, robust temporal constraints are not forthcoming. Locally, Artemis-radial fractures cut shield terrain material; elsewhere, shield terrain appears to cover Artemis-radial fractures. Shield terrain occurs in a broad band south of, and concentric to, Artemis Chasma. One possible mode of the formation of this unit is heating from below by the Artemis superplume, resulting in in situ partial melting of the overlying crust and emergence of point-source shield formation. It is possible that there is a spatial association, which might signal a genetic association, between ribbon-tessera terrain and shield terrain, but more focused research is required to evaluate this possibility.

Mahuea Tholus, southwestern AMA, forms a unique volcanic feature given its isolation from other volcanic features and fracture zones. Moore et al. (1992) suggested that Mahuea Tholus flows might be highly siliceous based on the texture of its flow surfaces and terminations, and its isolated location and high topography character relative to the adjacent lowlands. Whatever the composition of Mahuea Tholus flows, distal unit fMhb is deformed by Artemis-concentric wrinkle ridges. Thus, Mahuea was at least partially active prior to the latest stages of the Artemis superplume. However, flow emplacement of unit fMha, located in a proximal location, either postdated formation of the Artemis-concentric wrinkle-ridge suite or is rheologically unsuited to host wrinkle ridges.

The observation that Artemis-concentric wrinkle ridges cut numerous different material units—including shield terrain and flows clearly associated with individual coronae, mons, or tholi—indicates that this expansive suite of wrinkle ridges formed separate from the material units it cuts. This first-order observation invalidates characterization of a singular plains unit (or two) characterized by wrinkle ridges (e.g., Basilevsky & Head, 1998, 2000, 2002a, 2006; Ivanov & Head, 2011, 2015a, 2015b; Head, 2014), and the associated global stratigraphy (e.g., Basilevsky & Head, 1998, 2000, 2002b, 2006; Ivanov & Head, 2011, 2015a, 2015b; Head, 2014) and catastrophic resurfacing hypotheses (Armann & Tackley, 2012; Bullock et al., 1993; Dyar et al., 2018; Dyar & Smrekar, 2018; Gillmann & Tackley, 2014; Head, 2014; Ivanov & Head, 2015b; Moore et al., 2017; Nimmo & McKenzie, 1998; Strom et al., 1994).

The youngest regional-scale geological provinces and/or events within the AMA seem to be continued evolution of the Diana-Dali corona-chasma chain and the Vir-ava/Ralk-umgu chasma zone including Inari Corona. Both zones, which are generally along strike with one another, extend ~2,000 km in width and over 6,000 km in length and collectively define a zone marked by extensive tectonomagmatic activity (Bleamaster & Hansen, 2004). The Diana-Dali corona-chasma chain extends eastward to volcanic rise Atla Regio, which represents the surface expression of a large contemporary mantle plume (Hansen et al., 1997; Smrekar et al., 1997; Smrekar & Phillips, 1991). Atla Regio displays other tectonomagmatic fracture zones including Ganis Chasma, and the Hecate and Parga chasma-corona chains. Tectonic and magmatic activity along each of these spokes is likely genetically related to Atla Regio and thus of similarly young age (Bleamaster & Hansen, 2004; Hansen, 2018). The Diana-Dali zone is dominated by large coronae, yet this region is also affected by a pervasively developed fracture zone. Coronae within the Diana-Dali zone may have sourced early surface flows, or not; but more recent activity appears to have been tectonic in nature, marked by the development of radial and concentric fractures, and fractures parallel to the regional trend of the zone. Fractures (broadly defined) and hybrid structures characterize the Vir-ava/Ralk-umgu chasma zone;

fracture-fed flows are relatively rare, or rarely preserved, occurring mostly along the edges of zones of pervasive fracture development; the region is characterized by pervasively developed fractures broadly parallel to the regional trend of the host zone. As noted, the general lack of young surface flows across the Diana-Dali and Vir-ava/Ralk-umgu chasma zones is consistent with the development of topographically high and thin lithosphere (McGovern et al., 2015; Rosenblatt et al., 1994) or related to location within and adjacent to crustal plateaus and postulated thickened crust (Bleamaster & Hansen, 2004), or a mantle melt residuum root (Hansen, 2006). Further detailed study of this zone is warranted.

6. Conclusions

We conclude with a summary of a few first-order observations and/or geologic implications that emerge from the AMA geologic map.

1. Coherent patterns across the AMA define broad geologic domains, and broad cross-cutting temporal relationships, illustrating the evolution of this portion of Venus' surface through time. The three tectonic domains include, from oldest to youngest, (1) an ancient era characterized by ribbon-tessera terrain in both crustal plateaus and lowland inliers; (2) geologic units and structures associated with the development of the Artemis superstructure; and (3) the most recently formed fracture zone complex including associated corona-chasma chains.
2. Artemis-concentric wrinkle ridges cut numerous genetically different material units providing evidence that widespread units mapped by previous researchers, so-called plains with wrinkle ridges, actually represent multiple different units.
3. Artemis-radial fractures and Artemis-concentric wrinkle ridges defined regional patterns relative to Artemis Chasma (12,000- and ~13,000-km diameters, respectively) irrespective of the material units they define. These relations indicate that the wrinkle ridges are genetically related to an extremely large feature and not related to individual flows.
4. The Diana-Dali corona-chasma fracture zone broadly cross cuts the Artemis-radial fractures and -concentric wrinkle-ridge suites. These first-order relations provide robust temporal evidence that tectonic evolution of the Diana-Dali corona-chasma fracture zone outlasted "collapse" of the Artemis superplume.
5. Shield terrain, a unique style of volcanic unit first recognized and described by Aubele (1996) in Niobe Planitia, occurs as an extensive lithodemic terrain across the AMA in lowland locations. The evolution of this style of volcanism and the operative processes seem quite unique given the development of this type of terrain across huge regions, and yet the terrain is characterized by a thin surface layer marked by extremely local point-source volcanism. The volcanic and geodynamic significance of the unit remains a mystery worth further study.
6. Impact craters clearly formed time-transgressively across the AMA relative to each of the three major geologic eras noted above. Thus, there is no geologic evidence within the AMA that impact craters formed as the youngest "event" across the AMA; nor do geologic relations require temporally punctuated resurfacing of Venus. In fact, the range of temporal relations of impact craters provides evidence against catastrophic resurfacing hypotheses.
7. The fracture zone domain, the youngest and most spatially focused region of tectonomagmatic activity, postdated formation of 12% of the impact craters large enough to record relative geologic relations. This observation is consistent with the possibility that the fracture zone domain could represent ongoing geological activity.

In summary, the most first-order observation that emerges from the AMA is the regional coherence of preserved geologic patterns, which provide a variable record of three relatively distinct geologic eras: the ancient era, the Artemis superstructure era, and the youngest fracture zone complex era. The first two eras are also variably recorded within the NMA (Hansen & López, 2018; López & Hansen, 2020a, 2020b); all three eras can be extrapolated to the global scale, although the Artemis era is not strictly global as the Artemis superstructure covers about 30% of the planet surface (Hansen, 2018). Geologic relations captured within the AMA illustrate the spatial and temporal relations of these three eras across time and space as described herein. Future geologic mapping, at a similar scale of the other four IMap areas east of the AMA—south and north of the equator (Helen Planitia [I-2477] and Guinevere Planitia [I-2457],

respectively), and west of the AMA—south and north of the equator (Sedna Planitia [I-2466] and Lavinia Planitia [I-2475], respectively), will add important spatial and temporal information with regard to the evolution of these three geologic eras identified within the AMA. 1:10-M-scale mapping of these other regions, and the two polar 1:10-M cartographic sheets, might also lead to the identification of other geologic eras within the evolution of Earth's sister planet Venus.

Data Availability Statement

Base maps used for geologic mapping are available free in Zenodo (Hansen & López, 2020, http://doi.org/10.5281/zenodo.3769906). NASA Magellan data are available via USGS Map a Planet website (https://astrogeology.usgs.gov/tools/map-a-planet-2).

Acknowledgments
We thank reviewer I. Romeo and an anonymous reviewer for thoughtful reviews, and for helpful comments and guidance from editor Kirsty Tiampo. Geologic mapping was supported by National Aeronautics and Space Administration (NASA) (Award NNX12AQ71G). V. L. H. gratefully acknowledges support from the McKnight Foundation and the University of Minnesota. The authors have no financial conflicts of interests or other conflicts of interest with regard to this work.

References

Addington, E. A. (2001). A stratigraphic study of small volcano clusters on Venus. *Icarus*, *149*(1), 16–36. https://doi.org/10.1006/icar.2000.6529

Armann, M., & Tackley, P. J. (2012). Simulating the thermochemical magmatic and tectonic evolution of Venus's mantle and lithosphere: Two-dimensional models. *Journal of Geophysical Research*, *117*, E12003. https://doi.org/10.1029/2012JE004231

Arvidson, R. E., Baker, V. R., Elachi, C., Saunders, R. S., & Wood, J. A. (1991). Magellan: Initial analysis of Venus surface modification. *Science*, *252*(5003), 270–275. https://doi.org/10.1126/science.252.5003.270

Arvidson, R. E., Greeley, R., Malin, M. C., Saunders, R. S., Izenberg, N., Plaut, J. J., et al. (1992). Surface modification of Venus as inferred from Magellan observation of plains. *Journal of Geophysical Research*, *97*(E8), 13,303–13,317. https://doi.org/10.1029/92JE01384

Aubele, J. (1996). Akkruva small shield plains; definition of a significant regional plains unit on Venus. *LPSC*, *27*, 49–50.

Baker, V. R., Hamilton, C. W., Burr, D. M., Gulick, V. C., Komatsu, G., Luo, W., et al. (2015). Fluvial geomorphology on Earth-like planetary surfaces: A review. *Geomorphology*, *245*, 149–182. https://doi.org/10.1016/j.geomorph.2015.05.002

Baker, V. R., Komatsu, G., Gulick, V. C., & Parker, T. J. (1997). Channels and valleys. In S. W. Bougher, D. M. Hunten, & R. J. Phillips (Eds.), *Venus II—Geology, geophysics, atmosphere, and solar wind environment* (Vol. 1, pp. 13,395–13,420). Tucson, AZ: University of Arizona Press.

Baker, V. R., Komatsu, G., Parker, T. J., Gulick, V. C., Kargel, J. S., & Lewis, J. S. (1992). Channels and valleys on Venus—Preliminary analysis of Magellan data. *Journal of Geophysical Research*, *97*(E8), 13,421–13,444. https://doi.org/10.1029/92JE00927

Banerdt, W. B., McGill, G. E., & Zuber, M. T. (1997). Plains tectonics on Venus. In S. W. Bougher, D. M. Hunten, & R. J. Phillips (Eds.), *Venus II—Geology, geophysics, atmosphere, and solar wind environment* (Vol. 1, pp. 901–930). Tucson, AZ: University of Arizona Press.

Banks, B. K., & Hansen, V. L. (2000). Relative timing of crustal plateau magmatism and tectonism at Tellus Regio, Venus. *Journal of Geophysical Research*, *105*(E7), 17,655–17,667. https://doi.org/10.1029/1999JE001205

Bannister, R. A., & Hansen, V. L. (2010). Geologic map of the Artemis quadrangle (V-48), Venus. U.S. Geological Survey Scientific Investigations Map *3099*, 1:5M. http://pubs.usgs.gov/sim/3099/

Basilevsky, A. T., & Head, J. W. (1998). The geologic history of Venus: A stratigraphic view. *Journal of Geophysical Research*, *103*(E4), 8531–8544. https://doi.org/10.1029/98JE00487

Basilevsky, A. T., & Head, J. W. (2000). Geologic units on Venus: Evidence for their global correlation. *Planetary and Space Science*, *48*(1), 75–111. https://doi.org/10.1016/S0032-0633(99)00083-5

Basilevsky, A. T., & Head, J. W. (2002a). On rates and styles of late volcanism and rifting on Venus. *Journal of Geophysical Research*, *107*(E6), 5041. https://doi.org/10.1029/2000JE001471

Basilevsky, A. T., & Head, J. W. (2002b). Venus: Timing and rates of geologic activity. *Geology*, *30*, 1015–1018, doi:https://doi.org/10.1130/0091-7613 (2002)030<1015:VTAROG>2.0.CO;2.

Basilevsky, A. T., & Head, J. W. (2006). Impact craters on regional plains on Venus: Age relations with wrinkle ridges and implications for the geological evolution of Venus. *Journal of Geophysical Research*, *111*(E3), E03006. https://doi.org/10.1029/2005JE002473

Basilevsky, A. T., Head, J. W., Ivanov, M. A., & Kryuchkov, V. P. (1999). Impact craters on geologic units of northern Venus: Implications for the duration of the transition from tessera to regional plains. *Geophysical Research Letters*, *26*(16), 2593–2596. https://doi.org/10.1029/1999GL008329

Basilevsky, A. T., Head, J. W., Schaber, G. G., & Strom, R. G. (1997). The resurfacing history of Venus. In S. W. Bougher, D. M. Hunten, & R. J. Phillips (Eds.), *Venus II—Geology, geophysics, atmosphere, and solar wind environment* (Vol. 1, pp. 1047–1086). Tucson, AZ: University of Arizona Press.

Berthé, D., Choukroune, P., & Jegouzo, P. (1979). Orthogneiss, mylonite and noncoaxial deformation of granite—The example of the South Armoricain shear zone. *Journal of Structural Geology*, *1*(1), 31–42. https://doi.org/10.1016/0191-8141(79)90019-1

Bindschadler, D. L. (1995). Magellan—A new view of Venus geology and geophysics. *Reviews in Geophysics*, *33*, 459–467. https://doi.org/10.1029/95RG00281

Bindschadler, D. L., deCharon, A., Beratan, K. K., & Head, J. W. (1992). Magellan observations of Alpha Regio: Implications for formation of complex ridged terrains on Venus. *Journal of Geophysical Research*, *97*(E8), 13,563–13,577. https://doi.org/10.1029/92JE01332

Bjonnes, E. E., Hansen, V. L., James, B., & Swenson, J. B. (2012). Equilibrium resurfacing of Venus: Results from new Monte Carlo modeling and implications for Venus surface histories. *Icarus*, *217*(2), 451–461. https://doi.org/10.1016/j.icarus.2011.03.033

Bleamaster, L. F. III, & Hansen, V. L. (2004). Effects of crustal heterogeneity on the morphology of chasmata, Venus. *Journal of Geophysical Research*, *109*, E02004. https://doi.org/10.1029/2003JE002193

Bleamaster, L. F., III, & Hansen, V. L. (2005). Geologic map of the Ovda Regio quadrangle (V-35), Venus. U.S. Geological Survey Geologic Investigation Series Map *I-2802*, 1:5M. https://pubs.usgs.gov/imap/i2808/

Branney, M. J., Kokelaar, P., & Kokelaar, B. P. (2002). *Pyroclastic density currents and the sedimentation of ignimbrites*, *Geological Society Memoir* (Vol. 27), London: Geological Society of London.

Bullock, M. A., Grinspoon, D. H., & Head, J. W. (1993). Venus resurfacing rates: Constraints provided by 3-D Monte Carlo simulations. *Geophysical Research Letters*, *20*(19), 2147–2150. https://doi.org/10.1029/93GL02505

Bussey, D. B. J., Sorenson, S. A., & Guest, J. E. (1995). Factors influencing the capability of lava to erode its substrate: Application to Venus. *Journal of Geophysical Research*, *100*(E8), 16,941–16,948. https://doi.org/10.1029/95JE00894

Campbell, B. A. (1999). Surface formation rates and impact crater densities on Venus. *Journal of Geophysical Research*, *104*(E9), 21,951–21,955. https://doi.org/10.1029/1998JE000607

Campbell, B. A., & Campbell, D. B. (1992). Analysis of volcanic surface morphology on Venus from comparison of Arecibo, Magellan, and terrestrial airborne radar data. *Journal of Geophysical Research*, *105*(E10), 16,293–16,314.

Campbell, B. A., Campbell, D. B., Morgan, G. A., Carter, L. M., Nolan, M. C., & Chandler, J. F. (2015). Evidence of crater ejecta on Venus tessera terrain from Earth-based radar images. *Icarus*, *250*, 123–130. https://doi.org/10.1016/j.icarus.2014.11.025

Collins, G. C., Head, J. W., Basilevsky, A. T., & Ivanov, M. A. (1999). Evidence for rapid regional plains emplacement on Venus from the population of volcanically embayed impact craters. *Journal of Geophysical Research*, *104*(E10), 24,121–24,139. https://doi.org/10.1029/1999JE001041

Crumpler, L. S., Aubele, J. C., Senske, D. A., Keddie, T. D., Magee, K. P., & Head, J. W. (1997). Volcanoes and centers of volcanism on Venus. In S. W. Bougher, D. M. Hunten, & R. J. Phillips (Eds.), *Venus II—Geology, geophysics, atmosphere, and solar wind environment* (Vol. 1, pp. 697–756). Tucson, AZ: University of Arizona Press.

Cushing, G. E., Okubo, C. H., & Titus, T. N. (2015). Atypical pit craters on Mars. New insights from THEMIS, CTX, and HiRISE observations. *Journal of Geophysical Research: Planets*, *120*, 1023–1043. https://doi.org/10.1002/2014JE004735

DeShon, H. R., Young, D. A., & Hansen, V. L. (2000). Geologic evolution of southern Rusalka Planitia, Venus. *Journal of Geophysical Research*, *105*(E3), 6983–6995. https://doi.org/10.1029/1999JE001155

Dyar, D., & Smrekar, S. E. (2018). Venus: Our misunderstood sister, In AAS/Division for Planetary Sciences Meeting Abstracts (Vol. 50).

Dyar, D., Smrekar, S. E., & Glaze, L. S. (2018). The case for Venus. *Physics Today*. https://doi.org/10.1063/PT.6.3.20180323a

Easton, R. M., Edwards, L. E., Orndorff, R. C., Duguet, M., & Ferrusqua-Villafranca, I. (2016). North American commission on stratigraphic nomenclature North American Commission On Stratigraphic Nomenclature Report 12—Revision of article 37, Lithodemic units, of the North American Stratigraphic Code. *Stratigraphy*, *13*(3), 220–222.

Easton, R. M., Jones, J. O., Lenz, A. C., Ferrusqua-Villafranca, I., Mancini, E. A., Wardlaw, B. R., et al. (2005). North American commission on stratigraphic nomenclature. *AAPG Bulletin*, *89*(11), 1459–1464. https://doi.org/10.1306/05230505015

Ernst, R. E., Head, J. W., Parfitt, E., Grosfils, E., & Wilson, L. (1995). Giant radiating dyke swarms on Earth and Venus. *Earth-Science Reviews*, *39*(1–2), 1–58.

Ferrill, D. A., Wyrick, D. Y., Morris, A. P., Sims, D. W., & Franklin, N. M. (2004). Dilational fault slip and pit chain formation on Mars. *GSA Today*, *14*(10), 4–12. https://doi.org/10.1130/1052-5173(2004)014<4:DFSAPC>2.0.CO;2

Ford, J. P., & Plaut, J. J. (1993). Magellan image data. In J. P. Ford, et al. (Eds.), *Guide to Magellan image interpretation, National Aeronautics and Space Administration Jet Propulsion Laboratory Publication 93(24)* (pp. 7–18). Pasadena, CA: NASA JPL.

Ford, J. P., Plaut, J. J., & Parker, T. J. (1993). Volcanic features. In J. P. Ford, et al. (Eds.), *Guide to Magellan Image Interpretation, National Aeronautics and Space Administration Jet Propulsion Laboratory Publication 93(24)* (pp. 109–134). Pasadena, CA: NASA JPL.

Ford, J. P., Plaut, J. J., Weitz, C. M., Farr, T. G., Senske, D. A., Stofan, E. R., Michaels, G., & Parker, T. J. (1993). Guide to Magellan image interpretation. *National Aeronautics and Space Administration Jet Propulsion Laboratory Publication*, *93*(24), 148.

Ghail, R. C. (2002). Structure and evolution of southeast Thetis Regio. *Journal of Geophysical Research*, *107*(E8), 5060. https://doi.org/10.1029/2001JE001514

Ghent, R., & Hansen, V. (1999). Structural and kinematic analysis of eastern Ovda Regio, Venus: Implications for crustal plateau formation. *Icarus*, *139*(1), 116–136. https://doi.org/10.1006/icar.1999.6085

Gillmann, C., & Tackley, P. (2014). Atmosphere/mantle coupling and feedbacks on Venus. *Journal of Geophysical Research: Planets*, *119*, 1189–1217. https://doi.org/10.1002/2013JE004505

Gilmore, M. S., Collins, G. C., Ivanov, M. A., Marinangeli, L., & Head, J. W. (1998). Style and sequence of extensional structures in tessera terrain, Venus. *Journal of Geophysical Research*, *103*(E7), 16,813–16,840. https://doi.org/10.1029/98JE01322

Gilmore, M. S., & Head, J. W. (2018). Morphology and deformational history of Tellus Regio,Venus: Evidence for assembly and collision. *Planetary and Space Science*, *154*, 5–20. https://doi.org/10.1016/j.pss.2018.02.001

Gilmore, M. S., Ivanov, M. A., Head, J. W., & Basilevsky, A. T. (1997). Duration of tessera deformation on Venus. *Journal of Geophysical Research*, *102*(E6), 13,357–13,368. https://doi.org/10.1029/97JE00965

Gregg, T. K. P., & Greeley, R. (1993). Formation of venusian canali: Consideration of lava types and their thermal behaviors. *Journal of Geophysical Research*, *98*(E6), 10,873–10,882. https://doi.org/10.1029/93JE00692

Grosfils, E. B., & Head, J. W. (1994). The global distribution of giant radiating dike swarms on Venus: Implications for the global stress state. *Geophysical Research Letters*, *21*(8), 701–704. https://doi.org/10.1029/94GL00592

Guest, J. E., Bulmer, M. H., Aubele, J., Beratan, K., Greeley, R., Head, J. W., et al. (1992). Small volcanic edifices and volcanism in the plains of Venus. *Journal of Geophysical Research*, *97*(E10), 15,949–15,966. https://doi.org/10.1029/92JE01438

Guest, J. E., & Stofan, E. R. (1999). A new view of the stratigraphic history of Venus. *Icarus*, *139*(1), 55–66. https://doi.org/10.1006/icar.1999.6091

Hansen, V. L. (1992). Regional non-coaxial deformation on Venus—Evidence from western Izpapalotl Tessera. *LPSC XXIII*, 478–479.

Hansen, V. L. (2000). Geologic mapping of tectonic planets. *Earth and Planetary Science Letters*, *176*(3–4), 527–542. https://doi.org/10.1016/S0012-821X(00)00017-0

Hansen, V. L. (2002). Artemis: Surface expression of a deep mantle plume on Venus. *Geological Society of America Bulletin*, *114*(7), 839–848. https://doi.org/10.1130/0016-7606(2002)114<0839:ASEOAD>2.0.CO;2

Hansen, V. L. (2005). Venus's shield-terrain. *Geological Society of America Bulletin*, *117*(5), 808–822. https://doi.org/10.1130/B256060.1

Hansen, V. L. (2006). Geologic constraints on crustal plateau surface histories, Venus: The lava pond and bolide impact hypotheses. *Journal of Geophysical Research*, *111*(E11), E11010. https://doi.org/10.1029/2006JE002714

Hansen, V. L. (2018). Global tectonic evolution of Venus, from exogenic to endogenic over time, and implications for early Earth processes. *Philosophical Transactions of the Royal Society*, *376*(2132), 20170412. https://doi.org/10.1098/rsta.2017.0412

Hansen, V. L., & DeShon, H. R. (2002). Geologic map of the Diana Chasma Quadrangle (V-37), Venus. U.S. Geological Survey Geologic Investigations Series *I-27*

Hansen, V. L., & López, I. (2010). Venus records a rich early history. *Geology*, *38*(4), 311–314. https://doi.org/10.1130/G30587.1

Hansen, V. L., & López, I. (2014a). Southern Aphrodite fracture zone, Venus: Subsurface to surface volcano-tectonic connections, and a new mechanism for heat transfer. *Geological Society of America Abstracts with Programs*, *46*(6), 505.

Hansen, V. L., & López, I. (2014b). Hybrid fracture/dike/graben/pit-chain/canali structures on Venus: Dynamic interplay between surface and subsurface components of volcano-tectonic systems. *Geological Society of America Abstracts with Programs*, *46*(6), 563.

Hansen, V. L., & López, I. (2018). Mapping of geologic structures in the Niobe-Aphrodite map area of Venus: unraveling the history of tectonic regime change. *Journal of Geophysical Research: Planets*, *123*(7), 1760–1790. https://doi.org/10.1029/2018JE005566
Hansen, V. L., & López, I. (2020). Aphrodite region of Venus (I-2476): Base maps for geologic mapping. (data set). *Zenodo*, http://doi.org/10.5281/zenodo.3769906
Hansen, V. L., & Olive, A. (2010). Artemis, Venus: The largest tectonomagmatic feature in the solar system? *Geology*, *38*(5), 467–470. https://doi.org/10.1130/G30643.1
Hansen, V. L., & Phillips, R. J. (1993). Tectonics and volcanism of Eastern Aphrodite Terra: No subduction, no spreading. *Science*, *260*(5107), 526–530. https://doi.org/10.1126/science.260.5107.526
Hansen, V. L., Phillips, R. J., Willis, J. J., & Ghent, R. R. (2000). Structures in tessera terrain, Venus: Issues and answers. *Journal of Geophysical Research*, *105*(E2), 4135–4152. https://doi.org/10.1029/1999JE001137
Hansen, V. L., & Willis, J. J. (1996). Structural analysis of a sampling of tesserae: Implications for Venus geodynamics. *Icarus*, *123*(2), 296–312. https://doi.org/10.1006/icar.1996.0159
Hansen, V. L., & Willis, J. J. (1998). Ribbon terrain formation, southwestern Fortuna Tessera, Venus: Implications for lithosphere evolution. *Icarus*, *132*(2), 321–343. https://doi.org/10.1006/icar.1998.5897
Hansen, V. L., Willis, J. J., & Banerdt, W. B. (1997). Tectonic overview and synthesis. In S. W. Bougher, D. M. Hunten, & R. J. Phillips (Eds.), *Venus II—Geology, geophysics, atmosphere, and solar wind environment* (Vol. 1, pp. 797–844). Tucson, AZ: University of Arizona Press.
Hansen, V. L., & Young, D. A. (2007). Venus evolution: A synthesis. In M. Cloos, W. D. Carlson, M. C. Gilbert, J. G. Liou, & S. S. Sorensen (Eds.), *Convergent Marg Terranes and associated regions: A tribute to W.G. Ernst, Geological Society of America Special Paper* (Vol. 419, pp. 255–273). Denver: Geological Society of America. https://doi.org/10.1130/2006.2419(13
Hauck, S. A., Phillips, R. J., & Price, M. H. (1998). Venus: Crater distribution and plains resurfacing models. *Journal of Geophysical Research*, *103*(E6), 13,635–13,642. https://doi.org/10.1029/98JE00400
Head, J. W. (2014). The geologic evolution of Venus: Insights into Earth history. *Geology*, *42*(1), 95–96. https://doi.org/10.1130/focus012014.1
Head, J. W., & Wilson, L. (1991). Absence of large shield volcanoes and caldera on the Moon: Consequence of magma transport phenomena? *Geophysical Research Letters*, *18*(11), 2121–2124. https://doi.org/10.1029/91GL02536
Herrick, R. R., & Phillips, R. J. (1994). Implications of a global survey of Venusian impact craters. *Icarus*, *111*(2), 387–416. https://doi.org/10.1006/icar.1994.1152
Herrick, R. R., & Rumpf, M. E. (2011). Post impact modification by volcanic or tectonic processes as the rule, not the exception, for Venusian craters. *Journal of Geophysical Research*, *116*(E2), E02004. https://doi.org/10.1029/2010JE003722
Herrick, R. R., & Sharpton, V. L. (2000). Implications from stereo-derived topography of Venusian impact craters. *Journal of Geophysical Research*, *105*(E8), 20,245–20,262. https://doi.org/10.1029/1999JE001225
Herrick, R. R., Sharpton, V. L., Malin, M. C., Lyons, S. N., & Feely, K. (1997). Morphology and morphometry of impact craters. In S. W. Bougher, D. M. Hunten, & R. J. Phillips (Eds.), *Venus II—Geology, geophysics, atmosphere, and solar wind environment* (Vol. 1, pp. 1015–1046). Tucson, AZ: University of Arizona Press.
Ivanov, M. A., & Head, J. W. (2011). Global geological map of Venus. *Planetary and Space Science*, *59*(13), 1559–1600. https://doi.org/10.1016/j.pss.2011.07.008
Ivanov, M. A., & Head, J. W. (2015a). The history of tectonism on Venus: A stratigraphic analysis. *Planetary and Space Science*, *113*, 10–32.
Ivanov, M. A., & Head, J. W. (2015b). Volcanically embayed craters on Venus: Testing the catastrophic and equilibrium resurfacing models. *Planetary and Space Science*, *106*, 116–121. https://doi.org/10.1016/j.pss.2014.12.004
Izenberg, N. R., Arvidson, R. E., & Phillips, R. J. (1994). Impact crater degradation on Venusian plains. *Geophysical Research Letters*, *21*(4), 289–292. https://doi.org/10.1029/94GL00080
Janes, D. M., Squyres, S. W., Bindschadler, D. L., Baer, G., Schubert, G., Sharpton, V. L., & Stofan, E. R. (1992). Geophysical models for the formation and evolution of coronae on Venus. *Journal of Geophysical Research*, *97*(E10), 16,055–16,067. https://doi.org/10.1029/92JE01689
Jones, A. P., & Pickering, K. T. (2003). Evidence for aqueous fluid-sediment transport and erosional processes on Venus. *Journal of the Geological Society of London*, *160*(2), 319–327. https://doi.org/10.1144/0016-764902-111
Kerr, R. A. (1996). Does tellurium frost Venus's highlands? *Science*, *271*(5245), 28–29. https://doi.org/10.1126/science.271.5245.28
Kirk, R., Soderblom, L., & Lee, L. (1992). Enhanced visualization for interpretation of Magellan radar data—Supplement to the Magellan special issue. *Journal of Geophysical Research*, *97*(E10), 16,371–16,380. https://doi.org/10.1029/92JE01785
Komatsu, G., & Baker, V. R. (1994). Meander properties of venusian channels. *Geology*, *22*(1), 67–70. https://doi.org/10.1130/0091-7613(1994)022<0067:MPOVC>2.3.CO;2
Kreslavsky, M. A., Ivanov, M. A., & Head, J. W. (2015). The resurfacing history of Venus: Constraints from buffered crater densities. *Icarus*, *250*, 438–450. https://doi.org/10.1016/j.icarus.2014.12.024
Kumar, P. S. (2005). An alternative kinematic interpretation of Thetis Boundary Shear Zone, Venus. *Journal of Geophysical Research*, *110*(E7), E07001. https://doi.org/10.1029/2004JE002387
Lang, N. P., & Hansen, V. L. (2006). Venusian channel formation as a subsurface process. *Journal of Geophysical Research*, *111*(E4), E04001. https://doi.org/10.1029/2005JE002629
López, I., & Hansen, V. L. (2020a). Geologic map of the Niobe Planitia region (I-2467). *Venus*, *n/a*, n/a. https://doi.org/10.1002/essoar.10502475.1
López, I., & Hansen, V. (2020b). Geologic map of the Niobe Planitia region (I-2 467), Venus. *Earth and Space Science*, *7*(e2), https://doi.org/10.1029/2020EA001171
López, I., Lillo, J., & Hansen, V. L. (2008). Regional fracture patterns around volcanoes: Possible evidence for volcanic spreading on Venus. *Icarus*, *195*(2), 523–536. https://doi.org/10.1016/j.icarus.2007.12.026
McGovern, P. J., Grosfils, E. B., Galgana, G. A., Morgan, J. K., Rumpf, M. E., Smith, J. R., & Zimbelman, J. R. (2015). Lithospheric flexure and volcano basal boundary conditions: Keys to the structural evolution of large volcanic edifices on the terrestrial planets. In T. Platz, M. Massironi, P. K. Byrne, & H. Hiesinger (Eds.), *Volcanism and tectonism across the inner solar system* (Vol. 401, pp. 219–237). London: Geological Society Special Publications. https://doi.org/10.1144/SP401.7
McKinnon, W. B., Zahnle, K. J., Ivanov, B. A., & Melosh, H. J. (1997). Cratering on Venus—Models and observations. In S. W. Bougher, D. M. Hunten, & R. J. Phillips (Eds.), *Venus II—Geology, geophysics, atmosphere, and solar wind environment* (Vol. 1, pp. 969–1014). Tucson, AZ: University of Arizona Press.
Moore, H. J., Schenk, P. M., & Weitz, C. M. (1992). An explosive eruption on Venus. *LPSC Conference*, *23*, 927–928.

Moore, W. B., Simon, J. I., & Webb, A. A. G. (2017). Heat-pipe planet. *Earth and Planetary Science Letters*, *474*, 13–19. https://doi.org/10.1016/j.epsl.2017.06.015

Nimmo, F., & McKenzie, D. (1998). Volcanism and tectonics on Venus. *Annual Review of Earth and Planetary Sciences*, *26*(1), 23–51. https://doi.org/10.1146/annurev.earth.26.1.23

O'Rourke, J. G., & Korenaga, J. (2015). Thermal evolution of Venus with argon degassing. *Icarus*, *260*, 128–140. https://doi.org/10.1016/j.icarus.2015.07.009

O'Rourke, J. G., Wolf, A. S., & Ehlmann, B. L. (2014). Venus: Interpreting the spatial distribution of volcanically modified craters. *Geophysical Research Letters*, *41*, 8252–8260. https://doi.org/10.1002/2014GL062121

Okubo, C. H., & Martel, S. J. (1998). Pit crater formation on Kilauea volcano, Hawaii. *Journal of Volcanology and Geothermal Research*, *86*(1–4), 1–18. https://doi.org/10.1016/S0377-0273(98)00070-5

Parfitt, E. A., & Head, J. W. (1993). Buffered and unbuffered dike emplacement on Earth and Venus: Implications for magma reservoir size, depth, and rate of magma replenishment. *Earth, Moon, and Planets*, *61*(3), 249–281. https://doi.org/10.1007/BF00572247

Pettengill, G. H., Ford, P. G., & Simpson, R. A. (1996). Electrical properties of the Venus surface from bistatic radar observations. *Science*, *272*(5268), 1628–1631. https://doi.org/10.1126/science.272.5268.1628

Phillips, R. J. (1990). Convection-driven tectonics on Venus. *Journal of Geophysical Research*, *95*(B2), 1301–1316. https://doi.org/10.1029/JB095iB02p01301

Phillips, R. J., & Hansen, V. L. (1994). Tectonic and magmatic evolution of Venus. *Annual Review of Earth and Planetary Sciences*, *22*(1), 597–656. https://doi.org/10.1146/annurev.ea.22.050194.003121

Phillips, R. J., & Hansen, V. L. (1998). Geological evolution of Venus: Rises, plains, plumes, and plateaus. *Science*, *279*(5356), 1492–1497. https://doi.org/10.1126/science.279.5356.1492

Phillips, R. J., & Izenberg, N. R. (1995). Ejecta correlations with spatial crater density and Venus resurfacing history. *Geophysical Research Letters*, *22*(12), 1517–1520.

Phillips, R. J., Raubertas, R. F., Arvidson, R. E., Sarkar, I. C., Herrick, R. R., Izenberg, N., & Grimm, R. E. (1992). Impact craters and Venus resurfacing history. *Journal of Geophysical Research*, *97*(E10), 15,923–15,948. https://doi.org/10.1029/92JE01696

Plaut, J. J. (1993). Stereo imaging, in Guide to Magellan image interpretation. In J. P. Ford, et al. (Eds.), *Guide to Magellan image interpretation (National Aeronautics and Space Administration Jet Propulsion Laboratory Publication 93(24)* (33–41). Pasadena, CA: NASA JPL.

Price, M., & Suppe, J. (1994). Mean age of rifting and volcanism on Venus deduced from impact crater densities. *Nature*, *372*(6508), 756–759. https://doi.org/10.1038/372756a0

Price, M., & Suppe, J. (1995). Constraints on the resurfacing history of Venus from the hypsometry and distribution of volcanism, tectonism, and impact craters. *Earth, Moon, and Planets*, *71*(1–2), 99–145. https://doi.org/10.1007/BF00612873

Reese, C. C., Solomatov, V. S., & Orth, C. P. (2007). Mechanisms for cessation of magmatic resurfacing on Venus. *Journal of Geophysical Research*, *112*, E04S04. https://doi.org/10.1029/2006JE002782

Romeo, I. (2013). Monte Carlo models of the interaction between impact cratering and volcanic resurfacing on Venus: The effect of the Beta-Atla-Themis anomaly. *Planetary and Space Science*, *87*, 157–172. https://doi.org/10.1016/j.pss.2013.07.010

Romeo, I., Capote, R., & Anguita, F. (2005). Tectonic and kinematic study of a strike-slip zone along the southern margin of Central Ovda Regio, Venus—Geodynamical implications for crustal plateaux formation and evolution. *Icarus*, *175*(2), 320–334. https://doi.org/10.1016/j.icarus.2004.11.007

Romeo, I., & Turcotte, D. L. (2010). Resurfacing on Venus. *Planetary and Space Science*, *58*(10), 1374–1380. https://doi.org/10.1016/j.pss.2010.05.022

Rosenblatt, P., Pinet, P. C., & Thouvenot, E. (1994). Comparative hypsometric analysis of Earth and Venus. *Geophysical Research Letters*, *21*(6), 465–468. https://doi.org/10.1029/94GL00419

Schaber, G. G., Strom, R. G., Moore, H. J., Soderblom, L. A., Kirk, R. L., Chadwick, D. J., et al. (1992). Geology and distribution of impact craters on Venus—What are they telling us? *Journal of Geophysical Research*, *97*, 13,257–13,302.

Schaefer, L., & Fegley, B. (2004). Heavy metal frost on Venus. *Icarus*, *168*(1), 215–219. https://doi.org/10.1016/j.icarus.2003.11.023

Schaller, C. J., & Melosh, H. J. (1998). Venusian ejecta parabolas: Comparing theory with observations. *Icarus*, *131*(1), 123–137. https://doi.org/10.1006/icar.1997.5855

Schultz, P. H. (1992). Atmospheric effects on ejecta emplacement and crater formation on Venus. *Journal of Geophysical Research*, *97*(E10), 16,183–16,248. https://doi.org/10.1029/92JE01508

Schultz, R. A., Okubo, C. H., Goudy, C. L., & Wilkins, S. J. (2004). Igneous dikes on Mars revealed by Mars Orbiter Laser Altimeter topography. *Geology*, *32*(10), 889–892. https://doi.org/10.1130/G20548.1

Smrekar, S. E., Kiefer, W. S., & Stofan, E. R. (1997). Large volcanic rises on Venus. In I. S. W. Bougher, D. M. Hunten, & R. J. Phillips (Eds.), *Venus II—Geology, geophysics, atmosphere, and solar wind environment* (Vol. 1, pp. 845–879). Tucson, AZ: University of Arizona Press.

Smrekar, S. E., & Phillips, R. J. (1991). Venusian highlands: Geoid to topography ratios and their implications. *Earth and Planetary Science Letters*, *107*(3–4), 582–597. https://doi.org/10.1016/0012-821X(91)90103-O

Smrekar, S. E., & Stofan, E. R. (1997). Coupled upwelling and delamination: A new mechanism for corona formation and heat loss on Venus. *Science*, *277*(5330), 1289–1294. https://doi.org/10.1126/science.277.5330.1289

Smrekar, S. E., & Stofan, E. R. (1999). Origin of corona-dominated topographic rises on Venus. *Icarus*, *139*(1), 100–115. https://doi.org/10.1006/icar.1999.6090

Solomatov, V. S., & Moresi, L.-N. (1996). Stagnant lid convection on Venus. *Journal of Geophysical Research*, *101*(E2), 4737–4753. https://doi.org/10.1029/95JE03361

Solomon, S. C. (1993). The geophysics of Venus. *Physics Today*, *46*(7), 48–55. https://doi.org/10.1063/1.881359

Solomon, S. C., Smrekar, S. E., Bindschadler, D. L., Grimm, R. E., Kaula, W. M., McGill, G. E., et al. (1992). Venus tectonics: An overview of Magellan observations. *Journal of Geophysical Research*, *97*(E8), 13,199–13,255. https://doi.org/10.1029/92JE01418

Squyres, S. W., Janes, D. M., Baer, G., Bindschadler, D. L., Schubert, G., Sharpton, V. L., & Stofan, E. R. (1992). The morphology and evolution of coronae on Venus. *Journal of Geophysical Research*, *97*(E8), 13,611–13,634. https://doi.org/10.1029/92JE01213

Stofan, E. R., Brian, A. W., & Guest, J. E. (2005). Resurfacing styles and rates on Venus: Assessment of 18 Venusian quadrangles. *Icarus*, *173*(2), 312–321. https://doi.org/10.1016/j.icarus.2004.08.004

Stofan, E. R., & Guest, J. E. (2003). Geologic map of the Aino Planitia quadrangle (V–46), Venus: U.S. Geological Survey Geologic Investigations Series, I–2779, scale 1:5,000,000, https://pubs.usgs.gov/imap/i2779/

Stofan, E. R., Senske, D. A., & Michaels, G. (1993). Tectonic features in Magellan data. In J. P. Ford, et al. (Eds.), *Guide to Magellan image interpretation (National Aeronautics and Space Administration Jet Propulsion Laboratory Publication 93(24)* (93–108). Pasadena, CA: NASA JPL.

Stofan, E. R., Sharpton, V. L., Schubert, G., Baer, G., Bindschadler, D. L., Janes, D. M., & Squyres, S. W. (1992). Global distribution and characteristics of coronae and related features on Venus: Implications for origin and relation to mantle processes. *Journal of Geophysical Research*, *97*(E8), 13,347–13,378. https://doi.org/10.1029/92JE01314

Strom, R. G., Schaber, G. G., & Dawson, D. D. (1994). The global resurfacing of Venus. *Journal of Geophysical Research*, *99*(E5), 10,899–10,926. https://doi.org/10.1029/94JE00388

Tanaka, K. L., Skinner, J. A., & Hare, T. M. (2009). *Planetary geologic mapping handbook—2009*. U.S. Geological Survey.

Tovar, D., Hansen, V. L., & Swenson, J. B. (2015). Preliminary detailed structural map of an equatorial fracture zone (15S–20S/110E–124E), Western Aphrodite Terra, Venus. *LPSC*, *46*, 2555. pdf

Tuckwell, G. W., & Ghail, R. C. (2003). A 400-km-scale strike-slip zone near the boundary of Thetis Regio, Venus. *Earth and Planetary Science Letters*, *211*(1–2), 45–55. https://doi.org/10.1016/S0012-821X(03)00128-6

Turcotte, D. L. (1993). An episodic hypothesis for Venusian tectonics. *Journal of Geophysical Research*, *98*(E9), 17,061–17,068.

Turcotte, D. L., Morein, G., Roberts, D., & Malamud, B. D. (1999). Catastrophic resurfacing and episodic subduction on Venus. *Icarus*, *139*(1), 49–54. https://doi.org/10.1006/icar.1999.6084

U.S. Geological Survey (1998). Radar-image and shaded relief maps of the Aphrodite Planitia Region of Venus, 1:10,000,000. Map I-2476.

Watters, T. R. (1988). Wrinkle ridge assemblages on the terrestrial planets. *Journal of Geophysical Research*, *93*(10), 236–254.

Whitten, J. L., & Campbell, B. A. (2016). Recent volcanic resurfacing of Venusian craters. *Geology*, *44*(7), 519–522. https://doi.org/10.1130/G37681.1

Wietz, C. M. (1993). Impact craters. In J. P. Ford, et al. (Eds.), *Guide to Magellan image interpretation (National Aeronautics and Space Administration Jet Propulsion Laboratory Publication 93(24)* 75–92). Pasadena, CA: NASA JPL.

Wilhelms, D. E. (1972). *Geologic mapping of the second planet*, U.S. Geological Survey Interagency Report, Astrogeology.

Wilhelms, D. E. (1990). Geologic mapping, In R. Greeley and R. M. Batson (eds.), *Planetary mapping* (pp. 208–260). London: Cambridge University Press.

Williams-Jones, G., Williams-Jones, A. E., & Stix, J. (1998). The nature and origin of venusian canali. *Journal of Geophysical Research*, *3*, 8545–8555.

Wroblewski, F. B., Treiman, A. H., Bhiravarasu, S., & Gregg, T. K. (2019). Ovda Fluctus, the festoon lava flow on Ovda Regio, Venus: Not silica-rich. *Journal of Geophysical Research: Planets*, *124*, 2233–2245. https://doi.org/10.1029/2019JE006039

Zimbelman, J. R. (2001). Image resolution and evaluation of genetic hypotheses for planetary landscapes. *Geomorphology*, *37*(3–4), 179–199. https://doi.org/10.1016/S0169-555X(00)00082-9